

Error-Correcting Neural Networks for Semi-Lagrangian Advection in the Level-Set Method

Luis Ángel Larios-Cárdenas^{a,*}, Frédéric Gibou^{a,b}

^aComputer Science Department, University of California, Santa Barbara, CA 93106, USA

^bMechanical Engineering Department, University of California, Santa Barbara, CA 93106, USA

Abstract

We present a machine learning framework that blends image super-resolution technologies with scalar transport in the level-set method. Here, we investigate whether we can compute on-the-fly data-driven corrections to minimize numerical viscosity in the coarse-mesh evolution of an interface. The proposed system's starting point is the semi-Lagrangian formulation. And, to reduce numerical dissipation, we introduce an error-quantifying multilayer perceptron. The role of this neural network is to improve the numerically estimated surface trajectory. To do so, it processes localized level-set, velocity, and positional data in a single time frame for select vertices near the moving front. Our main contribution is thus a novel machine-learning-augmented transport algorithm that operates alongside selective redistancing and alternates with conventional advection to keep the adjusted interface trajectory smooth. Consequently, our procedure is more efficient than full-scan convolutional-based applications because it concentrates computational effort only around the free boundary. Also, we show through various tests that our strategy is effective at counteracting both numerical diffusion and mass loss. In passive advection problems, for example, our method can achieve the same precision as the baseline scheme at twice the resolution but at a fraction of the cost. Similarly, our hybrid technique can produce feasible solidification fronts for crystallization processes. On the other hand, highly deforming or lengthy simulations can precipitate bias artifacts and inference deterioration. Likewise, stringent design velocity constraints can impose certain limitations, especially for problems involving rapid interface changes. In the latter cases, we have identified several opportunity avenues to enhance robustness without forgoing our approach's basic concept. Despite these circumstances, we believe all the above assets make our framework attractive to parallel level-set algorithms. Its appeal resides in the possibility of avoiding further mesh refinement and decreasing expensive communications between computing nodes.

Keywords: machine learning, semi-Lagrangian advection, error modeling, neural networks, level-set method, Stefan problem

1. Introduction

The last few years have witnessed unprecedented progress in scientific disciplines thanks to machine learning. Advancements in these areas have sped up, especially with the democratization of computing resources and increased data accessibility. In particular, thriving machine learning applications [1–3] have emerged from computer vision and image processing [4–12], computer graphics [13], natural language processing and information retrieval [14–17], and sequencing and language translation [18–20]. Not long ago, machine learning and neural networks began carving their paths through the classic numerical methodologies, leading to promising ramifications in mathematics, physics, and engineering [21]. It all started with the groundbreaking work by Lagaris et al. [22, 23] to approximate the solution to boundary-value problems.

More recent machine learning incursions on computational science have brought about a broad spectrum of novel applications. Among these, physics-informed neural networks [24–26] have fueled a large body of scientific deep learning developments. The motivation behind them is to uncover the governing dynamics in spatiotemporal data sets

*Corresponding author

Email addresses: la1@cs.ucsb.edu (Luis Ángel Larios-Cárdenas), fgibou@ucsb.edu (Frédéric Gibou)

(e.g., [27, 28]). Also, another group of techniques has found a niche in conservation law simulations. Contributions in this branch include classifiers for near-discontinuity regions [29], shock detectors for complex flows [30], and under-resolved-stencil discriminators for surface reconstruction [31]. These models have assisted with balancing efficiency and accuracy by enabling their systems to switch between solvers depending on the field’s smoothness and other attributes.

Practitioners, too, have turned to machine learning to address challenging tasks in free-boundary problems (FBPs) [32]. Some implicit formulations widely used for solving FBPs are the volume-of-fluid (VOF) [33], the phase-field [34, 35], and the level-set methods [36]. In VOF technologies, we can find a representative combination of computational fluid dynamics (CFD) and machine learning in the work by Després and Jourdain with algorithms for bimaterial compressible Euler calculations [37]. Similarly, Qi et al. [38] and Patel et al. [39] have optimized neural networks to estimate curvature at the center of two- and three-dimensional volume-fraction stencils. Besides curvature computation, the interface geometry is likewise hard to characterize because of the discontinuous nature of the VOF representation. Ataei et al. [40], for example, have proposed a neural piece-wise linear interface reconstruction (NPLIC) system to deal with this difficulty. Their alternative approach has outperformed the complex analytical PLIC procedures [41] while being nearly as accurate at faster evaluation rates.

The level-set method has also benefited from data-driven technologies. In this formulation, researchers have actively sought efficacious solutions to long-standing difficulties derived from the absence of inbuilt mechanisms that secure well-balancedness [42] and preserve mass [43]. Such problems can get exacerbated in coarse meshes and when the free boundary undergoes severe stretching or tearing [44]. First, well-balancedness relates to surface tension models and their ability to recover equilibrium solutions [42]. It rests on estimating curvature accurately *at* the interface, regardless of mesh size. Although the level-set framework provides a straightforward relation to calculate curvature, it does not always yield satisfactory approximations when the level-set field lacks sufficient smoothness and regularity. With this in mind, we have recently proposed network-only [45] and hybrid inference systems [46] that tackle the curvature problem in low-resolution grids. Our investigation has revealed that blending traditional schemes with multilayer perceptrons produces better results than taking each component alone. In like manner, Buhendwa et al. [31] have developed a machine-learning interface-reconstruction (IR) strategy that computes volume fractions and apertures. Their procedure has proven effective for under-resolved regions and recovers the conventional IR for well-resolved sectors.

Often, artificial mass loss and numerical diffusion occur simultaneously. Further, the coarser the mesh, the more that one loses mass to under-resolution. Consequently, mesh refinement is the preferred option to minimize numerical dissipation. In order to refine a grid efficiently, researchers have proposed nonuniform discretization schemes to increase the resolution only next to the interface [47, 48]. Adaptive Cartesian grids, for instance, have served as the basis for high-order robust level-set algorithms and tools in both serial [49–55] and distributed computing systems [56, 57]. Over the years, practitioners have also combined level-set technologies with other numerical frameworks to improve mass conservation. Among these hybrid approaches, we can find the coupled level-set and volume-of-fluid [44], the particle level-set [58], the coupled volume-of-fluid and level-set [59], and the marker level-set [60] methods. Other computational scientists have opted for in-place augmentation by either adding volume reinitialization [61] or incorporating source/sink terms [62] into the standard formulation. However, little has been done to investigate mass loss from a data-driven perspective. In this manuscript, we bridge the level-set method with machine learning to offset numerical viscosity and preserve mass in low-resolution grids.

The present study draws inspiration from image super-resolution methodologies. The image super-resolution problem involves learning an end-to-end mapping between low- and high-resolution images [7]. In scientific computing, this concept is strongly connected with training low-resolution models to imitate the rules in their high-resolution counterparts [63, 64]. This idea, in particular, offers promising opportunities to circumvent the prohibitive costs of solving PDEs in grids with considerably small mesh sizes. In computer graphics, for instance, Xie et al. [13] have designed temporally coherent generative adversarial neural networks. Their networks learn to produce volumetric frames from a low-resolution field containing passively advected density and velocity data. Likewise, Liu et al. [65] have reconstructed turbulent flows from coarse spatiotemporal data with the aid of convolutional and multi-scale residuals blocks. Other influential developments in CFD include the learned discretizations of [63] and [64]. In [64], Zhuang et al. extend their data-driven discretizations in [63] to two-dimensional passive scalar advection in turbulent flows. Instead of using predefined finite-volume coefficients, Zhuang et al. have trained convolutional neural networks that emit optimal coefficients based on high-resolution simulations. Their machine learning approach thus helps to keep an exceptional level of accuracy, even when the solution is under-resolved with classic methods. In the same line, Pathak et al. [66] have developed a hybrid PDE-machine-learning strategy to enhance the accuracy of coarse,

high-Reynolds-number turbulent-flow simulations. Their framework’s key component is an *error-correcting* U-Net [9] convolutional network. This architecture helps restore fine-scale details in a high-resolution estimate of system variables and simultaneously corrects the error introduced during the coarse-grid simulation.

In this manuscript, we introduce a data-driven strategy that extends the notions in [64] and [66] to the level-set method. More precisely, we seek to minimize numerical viscosity in the coarse-mesh evolution of an interface to improve the accuracy of the solution to an FBP. To this end, we consider the semi-Lagrangian formulation [67–69] as our starting point. Semi-Lagrangian schemes are popular in the level-set community because of their unconditional stability and trivial nonuniform-grid implementation. Here, we blend these ordinary schemes with an error-quantifying neural network that corrects the numerically estimated surface trajectory. Unlike [64–66], our model is a plain multilayer perceptron. This network processes localized level-set, velocity, and positional data in a single time frame for select vertices near the moving front. Our main contribution is thus a novel machine-learning-augmented transport algorithm that operates alongside selective redistancing and alternates with standard advection to keep the adjusted interface trajectory smooth. Consequently, our procedure is more efficient than full-scan convolutional-based applications because it concentrates computational effort only around the free boundary. Also, we show through various tests that our strategy is effective at counteracting both numerical diffusion and mass loss. Some of these assessments reveal that our method can achieve the same precision as the baseline scheme at twice the resolution but at a fraction of the cost. Similarly, we prove that our hybrid technique can produce feasible solidification fronts for crystallization processes. In addition, our approach exhibits great generalization for simulation times that exceed the durations employed during training. When taken together, these assets make our framework attractive to parallel level-set algorithms. Its appeal resides in the possibility of avoiding further mesh refinement and decreasing expensive communications between computing nodes.

We have organized the paper as follows. Sections 2 to 4 provide background on the level-set method, quadtree Cartesian grids, and semi-Lagrangian advection schemes. Then, we state our methodology and related algorithms for training and deployment in Section 5. After these, Section 6 evaluates our approach through several standard tests cases. Finally, we conclude in Section 7, where we reflect on our results and limitations and offer diverse avenues for future work.

2. The level-set method

The level-set method [36] is an Eulerian formulation for capturing and tracking interfaces that undergo complex topological changes. The level-set representation denotes an interface by $\Gamma \doteq \{\mathbf{x} : \phi(\mathbf{x}) = 0\}$, where $\phi(\mathbf{x}) : \mathbb{R}^n \mapsto \mathbb{R}$ is a higher-dimensional, Lipschitz continuous relation known as the *level-set function*. In this framework, the zero-isocontour partitions the computational domain $\Omega \subseteq \mathbb{R}^n$ into the non-overlapping interior and exterior regions defined by $\Omega^- \doteq \{\mathbf{x} : \phi(\mathbf{x}) < 0\}$ and $\Omega^+ \doteq \{\mathbf{x} : \phi(\mathbf{x}) > 0\}$. Then, given some velocity field $\mathbf{u}(\mathbf{x})$, we can evolve $\phi(\mathbf{x})$ and Γ by solving the *level-set equation*:

$$\phi_t + \mathbf{u} \cdot \nabla \phi = 0. \quad (1)$$

Assuming that $\phi(\mathbf{x})$ remains sufficiently smooth after advection, one can use the following straightforward expressions to compute normal vectors and mean curvature for any point $\mathbf{x} \in \Omega$:

$$\hat{\mathbf{n}}(\mathbf{x}) = \frac{\nabla \phi(\mathbf{x})}{\|\nabla \phi(\mathbf{x})\|}, \quad \kappa(\mathbf{x}) = \nabla \cdot \frac{\nabla \phi(\mathbf{x})}{\|\nabla \phi(\mathbf{x})\|}. \quad (2)$$

When $\mathbf{u}(\mathbf{x})$ does not depend directly on $\phi(\mathbf{x})$, eq. (1) is linear, and we can solve it with a semi-Lagrangian approach [67, 68]. Compared with other numerical schemes, the semi-Lagrangian method is unconditionally stable. It is also trivial to implement on adaptive Cartesian grids, whereas higher-order advection solvers are challenging. Combining the semi-Lagrangian formulation with nonuniform meshes is thus convenient because it allows us to solve eq. (1) in level-set applications with very high grid resolutions.

In general, there is an infinite number of functions for which Γ describes the same zero-level-set. Usually, one chooses $\phi(\mathbf{x})$ to be a signed distance function to the interface because it simplifies computations (e.g., $\|\nabla \phi(\mathbf{x})\| = 1$) and helps to produce robust numerical results [70]. Also, signed distance functions are beneficial because they are uniquely determined as the viscosity solutions to the Eikonal equation [71]. Recent studies [45, 46] suggest that these functions can improve the accuracy of machine learning estimations, too. However, as a numerical simulation progresses, a signed distance function can deteriorate quickly, developing noisy features that compromise stability

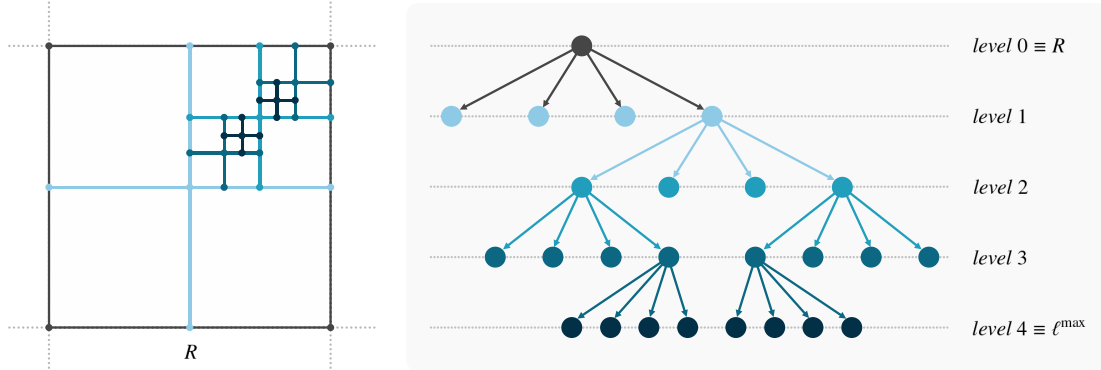


Figure 1: A (non-graded) quadtree Cartesian grid (left) and its data structure representation (right). The quadtree covers a region $R \subseteq \Omega$ corresponding to its root (*level 0*). We denote grid nodes as small dots at the intersections of the quadtree cells. (Color online.)

and precision. For this reason, it is customary to redistance $\phi(\mathbf{x})$ frequently by solving the pseudo-time transient *reinitialization equation* [70],

$$\phi_\tau + \text{sgn}(\phi^0)(\|\nabla\phi\| - 1) = 0, \quad (3)$$

where τ is a pseudo-time stepping variable, ϕ^0 is the starting level-set function, and $\text{sgn}(\cdot)$ is a smoothed-out signum function.

Typically, one uses a TVD Runge–Kutta scheme in time and a Godunov discretization in space to solve eq. (3) to steady-state (i.e., $\phi_\tau = 0$ and $\|\nabla\phi\| = 1$). For efficiency, we often stop this iterative process after a prescribed number of steps, ν , depending on the application and how close ϕ^0 is to a signed distance function. For a detailed description of the reinitialization algorithm, we refer the reader to the work of Min and Gibou [51] and Mirzadeh et al. [57]. In both cases, the authors redesigned the redistancing procedure for adaptive Cartesian grids, which we discuss in Section 3. For a complete presentation of the level-set technologies, the reader may consult Osher, Fedkiw, and Sethian’s classic texts [72, 73] and the latest review by Gibou et al. [74].

3. Adaptive Cartesian grids

Unlike uniform meshes, adaptive Cartesian grids significantly reduce the cost of solving FBP’s with level-set methods. They do so by increasing the spatial resolution only close to Γ , where more accuracy is needed [48]. In this work, we discretize a computational domain, Ω , with the help of standard quadtrees and signed distance level-set functions to digitize the corresponding grid \mathcal{G} .

A quadtree is a rooted data structure composed of discrete cells covering a rectangular region $R \subseteq \Omega$. A tree cell, C , either has four children (i.e., quadrants) or is a leaf [75]. Also, each cell contains a list with its vertex coordinates, nodal level-set values, and other application-dependent data. Figure 1 illustrates a quadtree with its cells organized into $0 \leq L = \ell^{\max} + 1$ levels. Given an L -level quadtree, we can perform several operations efficiently, like searching in $\mathcal{O}(\ln(\ell^{\max}))$ time and sorting [48]. In addition, we can determine the mesh size or minimum cell width, h , by establishing a relationship between Ω ’s side lengths and the maximum level of refinement ℓ^{\max} .

As with most level-set applications based on quadtree Cartesian grids, we have adopted Min’s extended Whitney decomposition [76] to refine the mesh near the zero-isocontour. To construct or update a quadtree, we begin at its root, R , and recursively subdivide its cells according to their distance to Γ until we reach level ℓ^{\max} . In particular, we mark cell C for refinement if the condition

$$\min_{v \in \text{vertices}(C)} |\phi(v)| \leq \text{Lip}(\phi) \cdot \text{diag}(C) \quad (4)$$

is valid, where v is a vertex, $\text{Lip}(\phi)$ is the level-set function’s Lipschitz constant (set to 1.2), and $\text{diag}(C)$ is C ’s diagonal length. Conversely, we mark any cells for coarsening whenever they cannot fulfill the above criterion [57].

Our research builds on the parallel level-set methods provided in [57], which rely on Burstedde and coauthors’ p4est library [56]. p4est is a suite of highly scalable routines for grid refinement, coarsening, partitioning, and load-balancing. This library represents the adaptive grid \mathcal{G} as a *forest* of abutting quadtrees rooted in individual cells of a

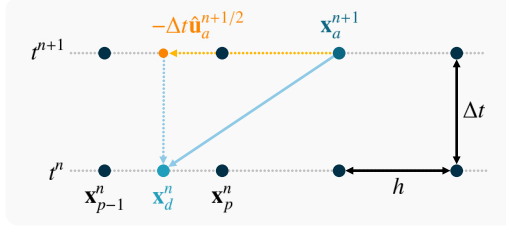


Figure 2: Illustration of backtracking with a one-dimensional semi-Lagrangian scheme. \mathbf{x}_a^{n+1} is the arrival grid point, \mathbf{x}_d^n is its departure point lying between \mathbf{x}_p^n and \mathbf{x}_{p-1}^n , and $\hat{\mathbf{u}}_a^{n+1/2}$ is the intermediate velocity from the midpoint method. The space-time characteristic trajectory appears as a light blue solid arrow and maps \mathbf{x}_a^{n+1} to \mathbf{x}_d^n . Adapted from [69]. (Color online.)

coarse parent grid known as the *macromesh*. The most important contribution of Mirzadeh et al. in [57] is a parallel interpolation procedure. This algorithm exploits p4est’s ghost layering and global nodal indexing by recreating the entire forest as a per-process, local hierarchical representation. As shown in Section 5, we extensively employ their local replication and multi-process interpolation mechanisms to realize semi-Lagrangian advection. For more details about p4est and the level-set methods for distributed memory systems using efficient MPI communications [77], we refer the reader to their respective manuscripts and handouts.

4. Semi-Lagrangian advection

Semi-Lagrangian schemes [68] are extensions of the Courant–Isaacson–Rees method [67]. Their convergence has been verified for several FBPs with passive transport, where eq. (1) is hyperbolic. For parabolic PDEs, where the Courant–Friedrichs–Lewy (CFL) condition requires $\Delta t \sim \mathcal{O}(h^2)$ for most explicit methods, semi-Lagrangian schemes can also converge with $\Delta t \sim \mathcal{O}(h)$ and the help of frequent reinitialization and velocity smoothing [48].

Because of their versatility, unconditional stability, and ease of implementation, practitioners have resorted to semi-Lagrangian methods for solving FBPs in both uniform and adaptive grids. Semi-Lagrangian schemes, however, are not conservative and often lead to mass loss when applied to the evolution of the level-set function [74]. The idea behind this numerical technique is to approximate the solution to eq. (1) by integrating the system

$$\begin{cases} \frac{dX(t)}{dt} = \mathbf{u}(X(t)) \\ \frac{d\phi(X(t), t)}{dt} = 0 \end{cases} \quad (5)$$

along the characteristic curves $X(t)$ backward in time. Thus, if \mathcal{G}^{n+1} is the computational grid at time $t^{n+1} = t^n + \Delta t$, we start at an *arrival* grid point \mathbf{x}_a^{n+1} lying on the trajectory X^{n+1} and trace it back to its *departure* point \mathbf{x}_d in the upwind direction. Then, we compute its level-set value as in [57] with

$$\phi^{n+1}(\mathbf{x}_a^{n+1}) = \phi^{n+1}(X^{n+1}) = \phi(X(t^{n+1}), t^{n+1}) = \phi(X(t^n), t^n) = \phi^n(X^n) = \phi^n(\mathbf{x}_d), \quad (6)$$

where the second-order accurate midpoint method provided in [51, 78],

$$\begin{aligned} \hat{\mathbf{x}} &= \mathbf{x}_a^{n+1} - \frac{\Delta t}{2} \mathbf{u}^n(\mathbf{x}_a^{n+1}) \\ \mathbf{x}_d &= \mathbf{x}_a^{n+1} - \Delta t \mathbf{u}^{n+\frac{1}{2}}(\hat{\mathbf{x}}), \end{aligned} \quad (7)$$

locates the departure point using the intermediate velocity

$$\mathbf{u}^{n+\frac{1}{2}} = \frac{3}{2} \mathbf{u}^n - \frac{1}{2} \mathbf{u}^{n-1}. \quad (8)$$

Since $\hat{\mathbf{x}}$ and \mathbf{x}_d do not necessarily coincide with grid points, we must interpolate the appropriate fields from \mathcal{G}^n and \mathcal{G}^{n-1} to calculate $\mathbf{u}^{n+\frac{1}{2}}(\hat{\mathbf{x}})$ and $\phi^n(\mathbf{x}_d)$. Figure 2 shows this situation in a one-dimensional example of the semi-Lagrangian scheme. In this work, we employ bilinear and quadratic interpolation to sample scalar and vector quantities

on quadtree Cartesian grids. As detailed by Strain in [48], if $C \in \mathcal{G}$ is an h -by- h quadtree cell with lower-left coordinates (x_0, y_0) , we can calculate $\phi(\mathbf{x})$ at $(x, y) = (x_0 + \alpha h, y_0 + \beta h) \in C$ using the piecewise bilinear interpolation form

$$\phi(x, y) = (1 - \alpha)(1 - \beta)\phi_{00} + (1 - \alpha)\beta\phi_{01} + (\alpha)(1 - \beta)\phi_{10} + (\alpha)\beta\phi_{11}, \quad (9)$$

where $\phi_{ij} = \phi(x_0 + ih, y_0 + jh)$ is a vertex value in C . Similarly, as noted by Min and Gibou in [51], we can get a quadratic interpolation procedure by correcting eq. (9) with second-order derivatives. Hence,

$$\begin{aligned} \phi(x, y) = & (1 - \alpha)(1 - \beta)\phi_{00} + (1 - \alpha)\beta\phi_{01} + (\alpha)(1 - \beta)\phi_{10} + (\alpha)\beta\phi_{11} \\ & - h^2 \frac{(\alpha)(1 - \alpha)}{2} \phi_{xx} - h^2 \frac{(\beta)(1 - \beta)}{2} \phi_{yy}, \end{aligned} \quad (10)$$

where ϕ_{xx} and ϕ_{yy} are bilinearly interpolated at (x, y) from their corresponding vertex values for C . The reader may consult [51] for more information about the standard finite-difference formulations to discretize ϕ_{xx} and ϕ_{yy} on non-graded adaptive meshes. In the present study, we have realized eqs. (9) and (10) with the technical implementation outlined in Algorithm 2 in [57] for heterogeneous computing systems.

5. Methodology

In this section, we state our data-driven strategy to improve the accuracy of semi-Lagrangian schemes in quadtree Cartesian grids. Our approach blends machine learning with the level-set technologies of [51] and [57] to solve a specialized instance of the image super-resolution problem [7]. The idea behind our framework stems from the fact that highly resolved grids yield much better solutions to FBPs than their coarser counterparts. Here, as in [66], we investigate the possibility of computing on-the-fly corrections for a coarse-grid interface trajectory so that it closely follows its corresponding evolution in a finer mesh.

5.1. Problem definition

Let \mathcal{S}^n be the state¹ of the solution to an FBP at time t^n . \mathcal{S} embodies a computational grid besides its nodal level-set, velocity, pressure, and temperature values, among others. Further, define `FBPEqnSolver()` as a sequence of nonlinear operators acting on \mathcal{S}^n . `FBPEqnSolver()` prepares the advection of $\phi^n \in \mathcal{S}^n$ by producing the intermediate state $\hat{\mathcal{S}}^n = \text{FBPEqnSolver}(\mathcal{S}^n)$. Then, given a time step Δt and a `SemiLagrangian()` procedure that performs the operations described in Section 4, the statement

$$\mathcal{S}^{n+1} = \text{SemiLagrangian}(\text{FBPEqnSolver}(\mathcal{S}^n), \Delta t) \quad (11)$$

finalizes the new solution at time t^{n+1} . In particular, the `SemiLagrangian()` method arrives at \mathcal{S}^{n+1} by advancing the sampled level-set function from ϕ^n to ϕ^{n+1} . Also, it updates the underlying quadtree Cartesian mesh from \mathcal{G}^n to \mathcal{G}^{n+1} . For a technical description of the `SemiLagrangian()` subroutine, the reader may consult Algorithm 3 in [57].

Next, consider a simulation that starts by discretizing Ω with a coarse mesh, \mathcal{G}_c^0 , and a fine mesh, \mathcal{G}_f^0 , where $\ell_c^{\max} < \ell_f^{\max}$ and $h_c > h_f$ (see fig. 1)². In addition, assume that the nodal coordinates in \mathcal{G}_c^n are a proper subset of the vertex coordinates in \mathcal{G}_f^n , $\forall t^n$. If $\mathcal{S}_c(t^0) = \mathcal{S}_f(t^0)$ is the FBP's initial condition³ involving the simultaneous coarse- and fine-grid solutions, then

$$\mathcal{S}_c(t^0 + \delta) = \text{SemiLagrangian}(\hat{\mathcal{S}}_c^0, \delta) \neq \text{SemiLagrangian}(\hat{\mathcal{S}}_f^0, \delta) = \mathcal{S}_f(t^0 + \delta) \quad (12)$$

after some finite time interval $\delta > 0$. More precisely, $\phi_c(t^0 + \delta) \neq \phi_f(t^0 + \delta)$ and $\Gamma_c(t^0 + \delta) \neq \Gamma_f(t^0 + \delta)$ mainly because of the numerical diffusion in the `SemiLagrangian()` function. Consequently, it is easy to anticipate that both the coarse- and the fine-grid solutions will diverge from each other as the simulation progresses.

¹We use the traditional shorthand temporal discretization $\psi^n \equiv \psi(t^n)$ for variable ψ .

²Unless otherwise stated, the subscript c refers to a coarse-grid feature/component and f to the fine-grid homologue.

³In practice, it suffices that $\mathcal{S}_c(t^0)$ and $\mathcal{S}_f(t^0)$ are approximately equal along a narrow region of interest (e.g., in a shell around Γ_c^0).

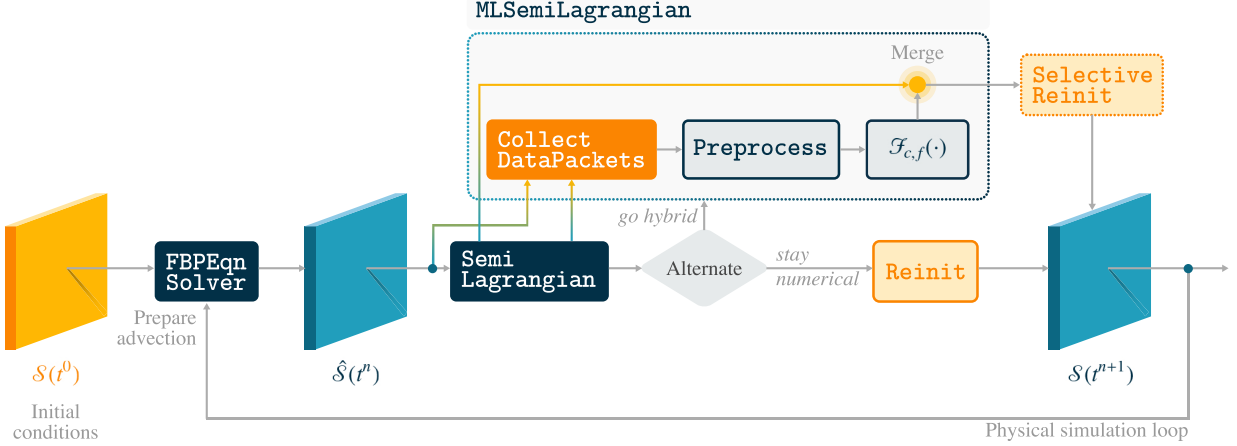


Figure 3: Overview of our hybrid semi-Lagrangian solver for FBPs. The `MLSemiLagrangian()` routine couples numerical advection with the error-correcting neural network $\mathcal{F}_{c,f}(\cdot)$ to improve the level-set accuracy of grid points lying next to Γ^n . A full description of `MLSemiLagrangian()` is provided in Algorithm 1. Our solver alternates between standard transport and machine-learning-induced advection. When using the neural model, we apply selective reinitialization to protect the level-set values in a subset of the corrected trajectory points. The alternating mechanism helps smooth out the level-set values near the evolving front since the `MLSemiLagrangian()` module cannot guarantee regularity on its own. (Color online.)

In this study, if $\bar{\delta} \sim \mathcal{O}(h_c)$ is a small time interval, and the velocity field satisfies $\max \|\mathbf{u}_c(\mathbf{x})\| = 1, \forall \mathbf{x} \in \Omega$, we posit that one can characterize $\mathcal{S}_c(t^0 + \bar{\delta})$'s deviation from $\mathcal{S}_f(t^0 + \bar{\delta})$ with

$$\phi_f(t^0 + \bar{\delta}) = \phi_c(t^0 + \bar{\delta}) + \bar{\varepsilon}, \quad (13)$$

where $\bar{\varepsilon}$ is the coarse level-set function error from the reference, high-resolution trajectory.

Therefore, if we can model $\bar{\varepsilon}$ in eq. (13) at regular intervals $\bar{\delta}$, we will be able to correct \mathcal{S}_c , improve its precision, and reduce artificial mass loss. As introduced in Section 3, we can further simplify this error model by concentrating our effort only at vertices next to Γ , where accuracy is critical.

5.2. Error-correcting neural networks for semi-Lagrangian advection

Our goal is to design a function that quantifies the *local error* $\bar{\varepsilon}$ incurred by $\phi_c^n(\mathbf{x})$'s semi-Lagrangian transport for any vertex next to the interface. In this model, we should leverage the statistical information available from various fields in $\hat{\mathcal{S}}_c^n$ in the neighborhood of Γ_c^n . Upon evaluating these fields, our function should estimate (with high precision) how much numerical dissipation in $\phi_c^{n+1}(\mathbf{x})$ has taken place as we advanced the simulation from t^n to t^{n+1} .

Let $\mathcal{F}_{c,f}(\cdot)$ be our *error-correcting* function for advected level-set values near Γ_c^n . Following state-of-the-art machine learning approaches in CFD [13, 64–66], here we have realized $\mathcal{F}_{c,f}(\cdot)$ as a neural network. More specifically, we resort to image super-resolution methodologies to estimate $\bar{\varepsilon}$. Consequently, we construct $\mathcal{F}_{c,f}(\cdot)$ by abstracting the difference between the coarse-mesh semi-Lagrangian advection of $\phi_c^n(\mathbf{x})$ and the numerical reference trajectory in a fine grid.

Figure 3 provides a simplified description of how $\mathcal{F}_{c,f}(\cdot)$ interacts with the components of a conventional FPB solver. The `MLSemiLagrangian()` block is the main contribution of this research. First, this module gathers special *data packets* from intermediate state information and `SemiLagrangian()`-advected level-set values for grid nodes near the interface at time t^n . Next, a custom subroutine preprocesses these packets and routes them to $\mathcal{F}_{c,f}(\cdot)$ for evaluation. Finally, $\mathcal{F}_{c,f}(\cdot)$ yields improved local estimations to $\phi_c^{n+1}(\mathbf{x})$ that are subsequently re-integrated to the `SemiLagrangian()` computations. The advection algorithm within the `MLSemiLagrangian()` method is iterative and involves successive mesh coarsening and refining steps until \mathcal{G}_c^{n+1} converges (see Section 3.2 in [57]). For efficiency, we cache the machine-learning-corrected level-set values from the first iteration. Then, we *merge* them with the proposed numerical estimations before each re-gridding operation. Besides the `MLSemiLagrangian()` unit, our framework includes a selective reinitialization function that masks out and protects a portion of the enhanced trajectory from the perturbations emerging when solving eq. (3). Figure 3 also depicts an *alternating mechanism* between standard advection and machine-learning-induced transport. Such a mechanism is fundamental to counteract the lack

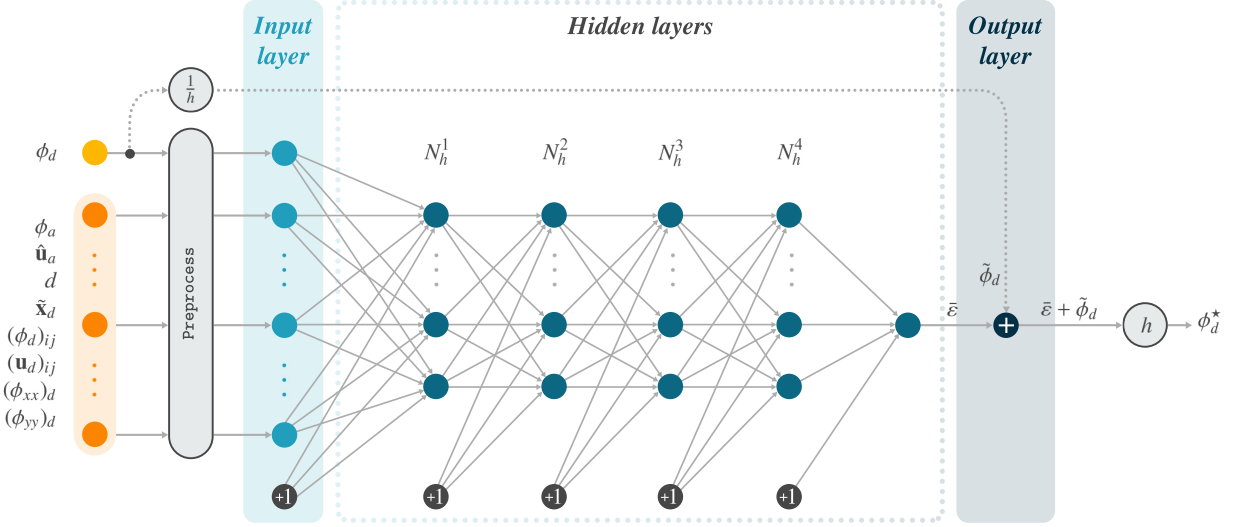


Figure 4: The error-correcting neural network, $\mathcal{F}_{c,f}(\cdot)$, employed in the `MLSemiLagrangian()` module of fig. 3. We also show the `Preprocess()` subroutine and the normalization/denormalization operations for the level-set value, ϕ_d , estimated with the semi-Lagrangian scheme of Section 4. In general, it is expected that the corrected output, ϕ_d^* , will be closer to the level-set value computed with a fine grid. (Color online.)

of physical constraints in $\mathcal{F}_{c,f}(\cdot)$ and regularize the adjusted level set values next to Γ_c^n . The following sections present how all these elements interplay in our hybrid advection system in more detail.

Our neural model resembles a localized version of the solver in [66] and adapts the hybrid strategy in [64] to the level-set framework. Figure 4 outlines $\mathcal{F}_{c,f}(\cdot)$'s architecture. Unlike [64, 66], $\mathcal{F}_{c,f}(\cdot)$ is an ordinary multilayer perceptron that outputs a corrected level-set value after digesting a small input vector. Besides a typical feedforward architecture for estimating $\bar{\epsilon}$, $\mathcal{F}_{c,f}(\cdot)$ features a skip connection that carries the h -normalized⁴ level-set value $\tilde{\phi}_d$ to a non-trainable additive neuron that computes $\bar{\epsilon} + \tilde{\phi}_d$. In the end, upon applying h -denormalization (subsumed in $\mathcal{F}_{c,f}(\cdot)$'s box in fig. 3), we produce a better level-set approximation, ϕ_d^* , for advancing the moving front. Compared to [65], $\mathcal{F}_{c,f}(\cdot)$ exploits only low-resolution data from one step, thus relieving the hybrid solver from buffering temporal information beyond time t^n . Figure 4 also displays the preprocessing module, which transforms incoming data according to patterns observed during training. Similar to our findings in [46], the `Preprocess()` subroutine is crucial for the `MLSemiLagrangian()` procedure because it favors learning convergence and increases $\mathcal{F}_{c,f}(\cdot)$'s accuracy. We discuss the `Preprocess()` building block alongside its technical implementation in Section 5.4.2.

Our goal is to ensure that the free boundary motion from Γ^n to Γ^{n+1} is highly accurate. For this reason, we reserve $\mathcal{F}_{c,f}(\cdot)$ for data packets collected for points \mathbf{x}_a^{n+1} lying next to the *known* interface at time t^n . As shown in fig. 4, the corresponding input for a qualified vertex \mathbf{x}_a^{n+1} to $\mathcal{F}_{c,f}(\cdot)$ is a preprocessed version of data usually available to the `SemiLagrangian()` subroutine. The latter is the basis to compute $\phi^{n+1}(\mathbf{x}_a^{n+1}) = \phi^n(\mathbf{x}_d)$. Among these data, we find level-set values, distances, velocity components, and second-order derivatives. All of them take the role of arguments in eqs. (6) to (10). Later, we describe data extraction in Section 5.3.

In order to specify a data packet formally, suppose we trace a vertex \mathbf{x}_a near Γ^n back to its departure point⁵, \mathbf{x}_d . To do so, we move in the $-\Delta t \hat{\mathbf{u}}_a$ direction according to eq. (7), where $\hat{\mathbf{u}}_a \equiv \mathbf{u}(\hat{\mathbf{x}}) \equiv \mathbf{u}^n(\hat{\mathbf{x}})$. The last expression follows since $\mathbf{u}^{n+\frac{1}{2}} \equiv \mathbf{u}^n$, and $\mathcal{F}_{c,f}(\cdot)$ does not consume entries from previous solution states. Furthermore, note that we have dropped the n superscript since all the admissible information (including the arrival point) belongs in the current time frame. Next, let C be the h -by- h square cell at the maximum level of refinement that *owns* \mathbf{x}_d . From C , we can build a data packet,

⁴For consistency, we indicate h -normalized variables with a tilde \sim accent.

⁵For data-packet specific data, we use the subscript a to denote information at the arrival point and d for the departure point.

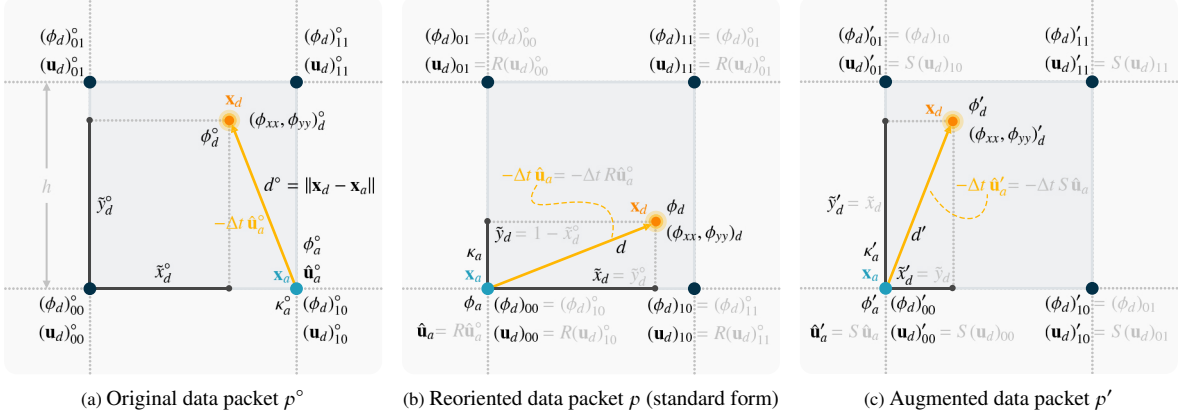


Figure 5: An h -by- h grid cell, C , at the maximum level of refinement owning the departure point, \mathbf{x}_d (in orange), for vertex \mathbf{x}_a (in light blue) lying next to Γ . Original sampled data from a numerical simulation appears in (a), denoted with a \circ superscript. Our inference system digests only numerical values shown in black. After reorientation, we obtain the machine-learning-suitable data packet in (b), where R is a rotation transformation (assuming that $\kappa_a^o < 0$). Invariant data to rotation transfers directly from (a) to (b), and we do not indicate any equality explicitly (e.g., $\phi_d = \phi_d^o$). (c) illustrates data augmentation by reflection about the line $y = x + \beta$, with $\beta \in \mathbb{R}$, going through \mathbf{x}_a . A permutation matrix S swaps the elements of multicomponent reoriented data in (b) (e.g., velocities). Invariant data to reflection transfers directly from (b) to (c) (e.g., $(\phi_d)'_{00} = (\phi_d)_{00}$). We denote augmented data with a prime superscript. (Color online.)

$$p = \left(\begin{array}{ll} \phi_a : & \text{level-set value at } \mathbf{x}_a \\ \hat{\mathbf{u}}_a : & \text{midpoint velocity at } \hat{\mathbf{x}} \\ d : & \text{distance from } \mathbf{x}_d \text{ to } \mathbf{x}_a \\ (\tilde{x}_d, \tilde{y}_d) : & \mathbf{x}_d \text{ coordinates w.r.t. } (x_0, y_0) \\ (\phi_d)_{ij} : & \text{nodal level-set values} \end{array} \quad \left(\begin{array}{ll} (\mathbf{u}_d)_{ij} : & \text{nodal velocities} \\ (\phi_{xx})_d : & \partial^2 \phi / \partial x^2 \text{ bilinearly interpolated at } \mathbf{x}_d \\ (\phi_{yy})_d : & \partial^2 \phi / \partial y^2 \text{ bilinearly interpolated at } \mathbf{x}_d \\ \kappa_a : & \text{curvature bilinearly interpolated at } \Gamma \\ \phi_d : & \text{numerical level-set value at } \mathbf{x}_d \end{array} \right) \in \mathbb{R}^{22}, \quad (14)$$

where $(\psi_d)_{ij} = (\psi_d)(x_0 + ih, y_0 + jh)$ is a vertex value with $i, j \in \{0, 1\}$, and (x_0, y_0) is C 's lower-left corner.

Figure 5a describes a data packet in a spatial context, where a \circ superscript differentiates the original from the *standard form* suitable for machine learning. Figure 5a also shows that \mathbf{x}_a always coincides with one of C 's vertices if we consider a unit *CFL* constant and a velocity maximum-unit-norm restriction. The previous statement about \mathbf{x}_a is true regardless of grid resolution and is essential for narrowing the problem at hand.

In earlier research [46], we exploited symmetry in the curvature problem to facilitate neural network design and data set composition. In particular, we confirmed that training only on the *negative curvature spectrum* encouraged efficiency, reduced architectural complexity, and sped up learning. These benefits hinged on the availability of inexpensive mechanisms to gauge a stencil's convexity and flip the sign of level-set values and inferred curvature accordingly. Here, we rely once more on this strategy to simplify $\mathcal{F}_{c,f}(\cdot)$'s topology while preserving, at least, the same expressive power as a full-curvature-spectrum model. Thus, the idea is to calculate κ_a^o in fig. 5a by discretizing eq. (2) using finite differences. Then, we estimate curvature at

$$\mathbf{x}_a^\Gamma = \mathbf{x}_a - \phi(\mathbf{x}_a) \frac{\nabla \phi(\mathbf{x}_a)}{\|\nabla \phi(\mathbf{x}_a)\|} \quad (15)$$

with bilinear interpolation. \mathbf{x}_a^Γ is a rough approximation for \mathbf{x}_a 's projection onto Γ^n . Next, we perform curvature-based normalization by negating p^o 's level-set values if $\kappa_a^o > 0$. After this step, we proceed to the last preparations before leaving the data packet in a well-suited form for the `Preprocess()` module. Finally, upon post-processing $\mathcal{F}_{c,f}(\cdot)$'s output in fig. 4, we check back κ_a^o and restore the sign for the machine-learning-corrected level-set value.

We have also resorted to *sample reorientation* to promote neural learning. This technique helps minimize feature variations and has proven effective in elementary computer vision applications, such as face recognition with *eigen-faces* [4, 79]. Figure 5b shows a data packet, p , after reorienting the original p^o , assuming that $\kappa_a^o < 0$. Putting p^o in standard form requires rotating it until the angle between the horizontal axis and $-\hat{\mathbf{u}}_a$ lies between 0 and $\pi/2$. Reorientation does not change intrinsic level-set values, curvature, and distance between \mathbf{x}_a and \mathbf{x}_d ; however, it affects vector quantities by pre-multiplying them with a rotation transformation $R(\theta)$, where $\theta = \pm k\pi/2$ and $k \in \{0, 1, 2\}$. After

reorientation, the arrival point becomes the origin of a local coordinate system that contains all the information we need in its first quadrant.

Following our description of the key features in the error-correcting multilayer perceptron, we next present the `MLSemiLagrangian()` procedure in Algorithm 1. This algorithm combines $\mathcal{F}_{c,f}(\cdot)$ with the parallel implementation of semi-Lagrangian schemes in [57]. Its formal parameters⁶ include $\mathcal{F}_{c,f}(\cdot)$, the quadtree data structure $\mathcal{G}^n \in \hat{\mathcal{S}}^n$, and the scalar/vector field vertex values necessary to construct the neural network inputs and advance the moving front. Further, Algorithm 1 assumes we have optimized $\mathcal{F}_{c,f}(\cdot)$ for reducing numerical diffusion in advected level-set values for nodes near Γ^n in a mesh with an ℓ_c^{\max} maximum level of refinement. Similar to its numerical counterpart, the `MLSemiLagrangian()` method produces new level-set values and updates the adaptive mesh. In addition, it generates an array of vertex coordinates that we should protect during selective reinitialization and where machine learning has been applied. As outlined above, the goal is to output nodal level-set values in ϕ^{n+1} with coordinates in \mathcal{C}^{n+1} closely resembling the free boundary motion in a higher-resolution grid.

Remark. We provide Algorithm 1 and the rest of the routines in the most general way. That is, we have used conventional formulae to determine the time step Δt based on a user-defined *CFL* constant and a possibly unbounded velocity field over Ω . However, to validate our assumptions and narrow down the learning problem, we have set $CFL = 1$ and $\max \|\mathbf{u}\| = 1$ for all nodes in \mathcal{G} . Therefore, as given by the first instruction of Algorithm 1, we have that $\Delta t = h$, and we can thus recover the data characterization provided in fig. 5.

The first step to incorporate machine learning into semi-Lagrangian advection in Algorithm 1 is to collect data packets in \mathcal{P} and their coordinates in \mathcal{C} for vertices next to Γ^n . To do so, we get the local forest hierarchical reconstruction \mathcal{H}^n and retrieve the information in eq. (14) and fig. 5a by calling `CollectDataPackets()`. We discuss `CollectDataPackets()` in some detail in Section 5.3. Then, we apply negative-curvature normalization and reorientation for each raw data packet $p \in \mathcal{P}$ to arrive at the standard form referenced in fig. 5b. At the same time, we populate the ancillary array \mathcal{S}_κ to record whether \mathbf{x}_a is proximal to a concave or convex interface region. For every machine-learning-suitable packet, we generate two samples: one with the preprocessed standard blob p and another with the augmented data packet p' . For example, fig. 5c illustrates the reflected data packet for the reoriented p shown in fig. 5b. The rationale for double-sampling is that the departure point’s level-set value does not change if we reflect its blob about a slope-one straight line going through the arrival point. By leveraging this invariance, we can increase the accuracy of ϕ_d^* if we average the predictions for the corresponding input samples

$$[\text{Preprocess}(p, h), \frac{1}{h}p \cdot \phi_d] \quad \text{and} \quad [\text{Preprocess}(p', h), \frac{1}{h}p' \cdot \phi_d]. \quad (16)$$

Notice that these samples are two-part input vectors that match $\mathcal{F}_{c,f}(\cdot)$ ’s expected format. Recently, practitioners have shown that such symmetry-preserving transformations and succeeding averaging can improve machine-learning IR in the level-set method [31]. Here, we realize these transformations with a few permutations over p ’s vertex values.

For efficiency, we allocate all the samples in matrix \mathcal{B} . Then, we launch $\mathcal{F}_{c,f}(\cdot)$ in batch mode to predict the h -normalized, error-corrected level-set values for the columns in \mathcal{B} . Upon h -denormalization, averaging, and sign-restoration using \mathcal{S}_κ , we recover the improved ϕ_d^* . Even though we anticipate ϕ_d^* will be more accurate than ϕ_d , outlying input patterns might lead to wild predictions in some scenarios. To account for these cases, we revert to ϕ_d whenever $\mathcal{F}_{c,f}(\cdot)$ predicts Γ^n should move by more than h or if the h -relative difference between ϕ_d and ϕ_d^* is over 15%. Neural network divergence is not uncommon in numerical experiments, and we have reported extreme cases when approximating mean curvature [46]. In this research, we mitigate such a vulnerability by taking uncomplicated precautions.

While collecting ϕ_d^* predictions, we simultaneously build a hash map, \mathcal{M}_ϕ , that links nodal coordinates to machine-learning-computed level-set values. \mathcal{M}_ϕ plays the role of a cache that prevents calling $\mathcal{F}_{c,f}(\cdot)$ more than once. Also, it is essential for data synchronization across processes and sharing what locally aware nodal ϕ_d^* values should persist after re-gridding. To instrument this map and update the ghost layer, we have used MPI [77], PETSc vectors [80], and the infrastructure in `p4est`[56].

The concluding part of Algorithm 1 merges the machine learning corrections with the discrete level-set function advected numerically in the rest of the mesh. The coupling occurs in an iterative process based on Algorithm 3 in [57]. In each iteration, we compute departure points, X_d , and their level-set values, ϕ^{n+1} , using eqs. (6) to (8) and

⁶For consistency, we represent one-element nodal variables as M -vectors in lowercase bold faces (e.g., ϕ^n) and variables with $d > 1$ values per node as d -by- M matrices in caps (e.g., U^n). M , in the `p4est` terminology, is the number of independent (locally owned and ghost) vertices that the quadtree data structure \mathcal{G}^n is aware of.

Algorithm 1: $(\mathcal{G}^{n+1}, \phi^{n+1}, \mathcal{C}^{n+1}) \leftarrow \text{MLSemiLagrangian}(\mathcal{F}_{c,f}(\cdot), \mathcal{G}^n, \phi^n, U^n, \Phi_{xx}^n, N^n, \kappa^n, CFL)$: Update level-set values ϕ^{n+1} from ϕ^n using a numerical semi-Lagrangian scheme with error correction provided by $\mathcal{F}_{c,f}(\cdot)$.

Input: error-correcting neural network for maximum coarse refinement level c and maximum fine refinement level f , $\mathcal{F}_{c,f}$; grid structure, \mathcal{G}^n ; nodal level-set values, ϕ^n ; nodal velocities, U^n ; level-set second spatial derivatives, Φ_{xx}^n ; nodal normal unit vectors, N^n ; nodal curvature values, κ^n ; CFL number.

Result: updated nodal structure, \mathcal{G}^{n+1} , nodal level-set values, ϕ^{n+1} , and array of coordinates updated with $\mathcal{F}_{c,f}(\cdot)$ to be protected with selective reinitialization, \mathcal{C}^{n+1} .

```

1   $h \leftarrow \mathcal{G}^n.\text{hmin}()$ ,  $\Delta t_\ell \leftarrow CFL \cdot h / \max \|U^n\|$ ; // Stepping variables
2   $\Delta t \leftarrow \text{MPI\_Allreduce}(\Delta t_\ell, \text{MPI\_MIN})$ ; // Retrieve minimum  $\Delta t$  across processes
3   $\mathcal{H}^n \leftarrow \text{Reconstruct}(\mathcal{G}^n)$ ; // Refer to Algorithm 1 in [57]

// Prepare computation of machine-learning-corrected level-set values for nodes next to  $\Gamma^n$ 
4   $(\mathcal{P}, \mathcal{C}) \leftarrow \text{CollectDataPackets}(\mathcal{G}^n, \mathcal{H}^n, \phi^n, U^n, \Phi_{xx}^n, N^n, \kappa^n, \Delta t)$ ; // See Algorithm 2
5   $\mathcal{S}_\kappa \leftarrow []$ ,  $\mathcal{B} \leftarrow []$ ; // List of true sample curvature signs and batch of network input samples
6  foreach data packet  $p \in \mathcal{P}$  do
7  |  $\mathcal{S}_\kappa.\text{append}(\text{Sign}(p.\kappa_a))$ ;
8  | transform  $p$ , so that  $p.\kappa_a$  is negative;
9  | rotate  $p$ , so that the angle of  $-p.\hat{\mathbf{u}}_a$  lies between 0 and  $\pi/2$ ;
   | // Produce two network input samples for each data packet to improve accuracy
10 |  $\mathcal{B}.\text{append}([\text{Preprocess}(p, h), \frac{1}{h}p.\phi_d])$ ;
11 | let  $p'$  be the reflected data packet about line  $y = x + \beta$  going through the arrival point;
12 |  $\mathcal{B}.\text{append}([\text{Preprocess}(p', h), \frac{1}{h}p'.\phi_d])$ ;
13 end

// Launch batch network predictions
14  $\mathcal{O} \leftarrow \mathcal{F}_{c,f}(\mathcal{B})$ ;

// Collect neural predictions and broadcast them across processes
15  $M_\phi \leftarrow \emptyset$ ; // Map of (local and ghost) node coordinates to  $\phi$  values computed with  $\mathcal{F}_{c,f}(\cdot)$ 
16 for  $l \leftarrow 0$  to  $(|\mathcal{P}| - 1)$  do
17 |  $\phi_d^* \leftarrow \frac{h}{2} (\mathcal{O}[2l] + \mathcal{O}[2l + 1])$ ; // Average neural prediction
18 | if  $\frac{1}{h} |\phi_d^* - \mathcal{P}[l].\phi_d| > 0.15$  or  $|\phi_d^* - \mathcal{P}[l].\phi_d| \geq h$  then
19 | |  $\phi_d^* \leftarrow \mathcal{P}[l].\phi_d$ ; // Catch possible divergence in neural prediction
20 | end
21 | fix sign of  $\phi_d^*$  according to  $\mathcal{S}_\kappa[l]$ ;
22 |  $M_\phi[\mathcal{C}[l]] \leftarrow \phi_d^*$  only if  $\phi_d^*$  did not revert to numerical approximation;
23 end
24  $\text{UpdateGhostValues}(M_\phi)$ ; // Use MPI to gather values for ghost nodes updated via  $\mathcal{F}_{c,f}(\cdot)$ 

// Couple machine-learning-corrected trajectory with the rest of the level-set values
25  $\mathcal{G}_0^{n+1} \leftarrow \mathcal{G}^n$ ;
26 while true do
27 |  $X_d \leftarrow \text{ComputeDeparturePoints}(\mathcal{G}_0^{n+1}, U^n, \Delta t)$ ; // Using eqs. (7) and (8)
28 |  $\phi^{n+1} \leftarrow \text{Interpolate}(\mathcal{H}^n, \phi^n, X_d)$ ; // Refer to Algorithm 2 in [57]
29 |  $\text{AdjustLevelSetWithMLSolution}(\phi^{n+1}, M_\phi)$ ; // Correct  $\phi$  for nodes with coordinates in  $M_\phi$ 
30 |  $\mathcal{G}^{n+1} \leftarrow \mathcal{G}_0^{n+1}.\text{refineAndCoarsen}(\phi^{n+1})$ ; // Using criterion in eq. (4)
31 | if  $\mathcal{G}^{n+1} \neq \mathcal{G}_0^{n+1}$  then
32 | |  $\mathcal{G}^{n+1}.\text{partition}()$ ;
33 | |  $\mathcal{G}_0^{n+1} \leftarrow \mathcal{G}^{n+1}$ ;
34 | else
35 | | break;
36 | end
37 end

38  $\mathcal{W}^{n+1} \leftarrow \text{GetCoordsWithNegativeFlow}(\mathcal{H}^n, U^n, N^n, \mathcal{G}^{n+1}, \phi^{n+1})$ ; // Points 'lagging behind'  $\Gamma^{n+1}$ 
39  $\mathcal{C}^{n+1} \leftarrow M_\phi.\text{getListOfKeys}() \cap \mathcal{W}^{n+1}$ ; // Vertices to protect during reinitialization
40 return  $(\mathcal{G}^{n+1}, \phi^{n+1}, \mathcal{C}^{n+1})$ ;

```

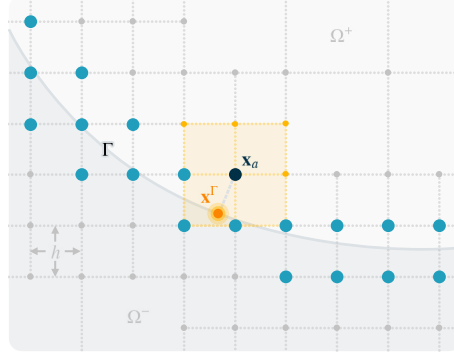


Figure 6: A set of sampled nodes adjacent to a concave interface region in a quadtree Cartesian mesh. Vertices with full h -uniform, nine-point stencils appear in light blue. We gather these nodes with the help of the `GetLocalNodesNextToGamma()` subroutine inside Algorithm 2. Among them, we shade in yellow the stencil of the (arrival) grid point \mathbf{x}_a colored in dark blue. We denote the rough estimation to the closest point on Γ to \mathbf{x}_a as \mathbf{x}^Γ (shown in orange). (Color online.)

interpolation from data at time t^n . The `Interpolate()` method entails a series of distributed actions that rely on synchronization and \mathcal{H}^n to retrieve scattered information from different sites. Then, we replace the numerical level-set values with the machine-learning ones in \mathcal{M}_ϕ for independent nodes whose coordinates match some key in the cache. Last, we refine and coarsen the candidate new grid to produce \mathcal{G}^{n+1} according to the criterion in eq. (4). We execute these operations repeatedly until \mathcal{G}^{n+1} converges. Usually, convergence requires no more steps than the maximum number of subdivisions in any quadtree [57].

Upon exiting the update loop, we gather the vertex coordinates in \mathcal{M}_ϕ and intersect them with \mathcal{W}^{n+1} , which results from calling `GetCoordsWithNegativeFlow()`. This ancillary subroutine locates vertices within a narrow band of half-width $2h\sqrt{2}$ around Γ^{n+1} , where the angular condition

$$\text{acos}\left(-\text{sign}\left(\phi^{n+1}(\mathbf{x})\right)\hat{\mathbf{n}}^n(\mathbf{x})\cdot\hat{\mathbf{u}}^n(\mathbf{x})\right)\leq\theta_W \quad (17)$$

holds for $\theta_W = 19\pi/36 = 95^\circ$. In this expression, \mathbf{x} is a point in \mathcal{G}^{n+1} , and $\hat{\mathbf{n}}$ and $\hat{\mathbf{u}}$ are the normal and velocity unit vectors interpolated from data at time t^n . Intuitively, eq. (17) selects nodes lagging behind the motion of the new interface. The goal is to protect enhanced level-set values in ϕ^{n+1} from indiscriminate redistancing on points lying on one side of Γ^{n+1} at the current iteration. Then, we resort to the conventional semi-Lagrangian scheme to smooth out the moving front from the opposite side at time t^{n+2} . In other words, improving the free boundary trajectory is not a task of the `MLSemiLagrangian()` function alone; it demands a delicate balance between machine learning correction, selective reinitialization, and alternating purely numerical advection. As we show in Section 5.4, such a technique is used not only at the inference stage but also during training.

5.3. Data-packet collection for learning and inference

The `CollectDataPackets()` subroutine in Algorithm 2 is a simple procedure that exploits the multi-process interpolation mechanism of [57] to extract information from local cells owning departure points. This information is necessary during inference (see Algorithm 1) and when constructing the training data set (see Section 5.4).

We begin Algorithm 2 by extracting a set of locally owned nodes, \mathcal{N} , near Γ . Every node $n \in \mathcal{N}$ with coordinates $n.\mathbf{x} = (n.x, n.y)$ has a full h -uniform, nine-point stencil and satisfies at least one of the four conditions: $\phi(n.x, n.y) \cdot \phi(n.x \pm h, n.y) \leq 0$ or $\phi(n.x, n.y) \cdot \phi(n.x, n.y \pm h) \leq 0$. Figure 6 portrays a group of vertices typically found in \mathcal{N} .

For each node $n \in \mathcal{N}$, first, we compute its departure point, \mathbf{x}_d , and midpoint velocity, $\hat{\mathbf{u}}$, with eqs. (7) and (8). Next we use \mathbf{x}_d and $\hat{\mathbf{u}}$ to check the validity of n and decide if we should continue processing it. A grid node is valid when its intermediate velocity is nonzero, and its departure point lies within a cell, $C \in \Omega$, at the maximum level of refinement. Besides the *CFL* and velocity-norm restrictions, these new constraints help confine the problem's complexity and promote data consistency.

After validation, we fetch a partially populated blob p using the information available for n in cell C . To do so, we resort to the `FetchDataPacket()` subroutine, which is a specialization of the multi-process `Interpolate()` function. Upon calling `FetchDataPacket()`, p will hold data for $(\tilde{x}_d, \tilde{y}_d)$, $(\phi)_{ij}$, $(\mathbf{u}_d)_{ij}$, $(\phi_{xx})_d$, and $(\phi_{yy})_d$. Then, we fill in the missing fields in p by computing n 's distance d from \mathbf{x}_d and querying its nodal level-set value ϕ_a . In addition, we

Algorithm 2: $(\mathcal{P}, \mathcal{C}) \leftarrow \text{CollectDataPackets}(\mathcal{G}, \mathcal{H}, \phi, U, \Phi_{xx}, N, \kappa, \Delta t)$: Collect data packets for nodes next to Γ .

Input: grid structure, \mathcal{G} ; tree hierarchy, \mathcal{H} ; nodal level-set values, ϕ ; nodal velocities, U ; level-set second spatial derivatives, Φ_{xx} ; nodal normal unit vectors, N ; nodal curvature values, κ ; time step, Δt .

Result: array of data packets, \mathcal{P} ; array of coordinates, \mathcal{C} .

```

1  $\mathcal{N} \leftarrow \text{GetLocalNodesNextToGamma}(\mathcal{G}, \phi)$ ;
2  $\mathcal{P} \leftarrow []$ ,  $\mathcal{C} \leftarrow []$ ;
3 foreach node  $n \in \mathcal{N}$  do
4    $(\mathbf{x}_d, \hat{\mathbf{u}}) \leftarrow \text{ComputeDeparturePointAndMidVel}(\mathcal{G}, U, n, \Delta t)$ ; // Using eqs. (7) and (8)
5   if  $\|\hat{\mathbf{u}}\| \leq \epsilon$  or  $\text{IsValid}(\mathcal{G}, \mathbf{x}_d)$  then skip node  $n$ ;
6    $p \leftarrow \text{FetchDataPacket}(\mathcal{H}, \phi, \Phi_{xx}, \mathbf{x}_d, h)$ ; // Populate most of  $p$  data via interpolation
   // Fill in missing information in  $p$ 
7    $p.d \leftarrow \|\mathbf{x}_d - n.\mathbf{x}\|$ ; // Distance between arrival and departure points
8    $p.\hat{\mathbf{u}}_a \leftarrow \hat{\mathbf{u}}$ ; // Midpoint velocity used at arrival point
9    $p.\phi_a \leftarrow \phi[n]$ ; // Level-set value at arrival point
10   $\mathbf{x}^\Gamma \leftarrow n.\mathbf{x} - \phi[n](N[n])$ ; // Using eqs. (2) and (15)
11   $p.\kappa_a \leftarrow \text{Interpolate}(\mathcal{H}, \kappa, \mathbf{x}^\Gamma)$ ; // Curvature at closest point to  $n.\mathbf{x}$  on  $\Gamma$ 
12   $\mathcal{P}.\text{append}(p)$ ;
13   $\mathcal{C}.\text{append}(n.\mathbf{x})$ ;
14 end
15 return  $(\mathcal{P}, \mathcal{C})$ ;

```

bilinearly interpolate curvature at n 's projection on Γ , as specified by eq. (15). Once more, note that our interpolative tasks require a local hierarchical reconstruction, \mathcal{H} , to determine which partition owns \mathbf{x}_d . For a detailed description of the distributed interpolation procedure, we refer the reader to Algorithm 2 in [57]. By the end of our Algorithm 2, we will have all the valid-vertex data packets in \mathcal{P} and their respective coordinates (i.e., arrival points) in \mathcal{C} .

5.4. Training

The motivation for developing the error-correcting neural network originates in the promising results from machine learning applications that rest on image super-resolution methodologies [7, 13, 63–66]. Under these paradigms, to recover the information lost on a low-resolution grid, one should solve the same problem on a highly resolved mesh and assess the difference between both systems. In other words, the coarse-grid solution should mimic the fine-grid solution as much as possible with the help of the available data. In our case, we have already stated what information we can leverage when tracking the evolution of a moving front. Therefore, to train $\mathcal{F}_{c,f}(\cdot)$, we must assemble a data set, \mathcal{D} , with curated low-resolution input data packets and high-resolution (departure) output target level-set values. Later, we can contrast the inferred ϕ_d^* values in fig. 4 with their reference counterparts to optimize $\mathcal{F}_{c,f}(\cdot)$ via gradient descent.

5.4.1. Data-set generation

First, we explain how to build the learning data set \mathcal{D} . The high-level recipe is straightforward as long as we consider just one coarse resolution at a time. If various mesh sizes are necessary, one must produce their corresponding data sets separately and train their respective neural networks. This idea would be the semi-Lagrangian-scheme equivalence to the curvature neural-network dictionaries introduced in previous studies [45, 46]. Now, assuming that we discretize Ω with adaptive Cartesian grids, let ℓ_c^{\max} and ℓ_f^{\max} be the coarse- and fine-mesh maximum levels of refinement (refer to fig. 1). As stated in Section 5.1, we presume that $\ell_c^{\max} < \ell_f^{\max}$ and $h_c > h_f$. Thus, to populate \mathcal{D} , it suffices to set up a *direct numerical simulation* (DNS) with a predefined level-set function. Then, one must advect its interface simultaneously on a coarse and a fine grid with an external velocity field and collect samples periodically until some ending time. To accommodate the alternating mechanism described in Section 5.2 and illustrated in fig. 3, we note that data collection takes place every other iteration. Furthermore, we can promote pattern variation and generalization if we repeatedly perform these steps for random configurations. This randomization technique is the backbone of the `GenerateDataSet()` procedure presented in Algorithm 3.

Algorithm 3 is combinatorial. For each velocity field, we draw a level-set-function base parameter from a range of evenly distributed values. Then, we spawn the proper initial level-set configuration at N_C different places within the

computational domain. For simplicity, we use circular-interface level-set functions whose base parameters are their radii, and initial configurations are their interface centers. In our case, $N_F = 7$ velocity fields and $N_C = 4$ locations per radius yield sufficiently large data sets from simulations that last up to $t^{end} = 0.5$. Also, to minimize concurrency issues, we carry out Algorithm 3 in a uni-process system that can fit a computational 2-by-2 discretized $\Omega \equiv [-1, +1]^2$ with four unit-square quadtrees.

As mentioned before, if $CFL = 1$ and $\max \|\mathbf{u}(\mathbf{x})\| = 1, \forall \mathbf{x} \in \Omega$, all nodes of interest will coincide with one vertex in their departure-point-owning cells (see fig. 5). By enforcing this constraint, we ensure that those departure points never lie farther than two cells away from Γ^n . Consequently, it is enough to require a coarse-grid uniform band around Γ^n of half-width $B_c = 2$ (measured in cell diagonals) in anticipation of Algorithm 2’s validity test. For accuracy, we also impose a uniform band of half-width B_f in the fine grid. While B_c aids with data consistency and problem simplification, B_f favors precision when querying target level-set values. In particular, B_f is relevant to how we interleave advection of low- and high-resolution level-set values: first, we advance the fine-grid level-set function; then, we use that updated trajectory to determine which reference (i.e., more accurate) level-set values should become targets to the sampled coarse-grid arrival points. Therefore, if Δt_c is the coarse time step, the advected-fine-mesh band around $\Gamma_f(t^n + \Delta t_c)$ must be wide enough to encompass the coarse-grid selected nodes at time t^n . The expression for setting B_f in the preamble of Algorithm 3 reassures these properties and a bit more. Since we have discretized Ω with unit-square Cartesian quadtrees, the ratio from coarse to fine mesh size, $h_c : h_f$, is a power of two. Accordingly, after advecting the high-resolution level-set function, we find that the sampled coarse-grid points overlap with vertices within the uniform band around the new fine-grid zero-isocontour. The latter is a desirable feature when assembling \mathcal{D} , considering that we use interpolation to fetch information from the fine and into the coarse mesh.

Following the initialization of h_c and h_f , we set the bounds for the interface radius. With these mesh sizes, we also define N_r , which is the number of radii to evaluate for every velocity field. Here, N_r is equivalent to over three times as many coarse cells fit between r_{\max} and r_{\min} . Then, we enter the outermost data production loop, where we repeatedly generate divergence-free, random velocity fields $\mathcal{V}_i(\mathbf{x})$, for $i = 1, 2, \dots, N_F$. In this study, we have realized $\mathcal{V}_i(\mathbf{x})$ as superpositions of sinusoidal waves [81], as implemented by [63] and [64]. Subsequently, we normalize these fields so that $\max \|\mathcal{V}_i(\mathbf{x})\| = 1$.

After defining $\mathcal{V}_i(\mathbf{x})$, we instantiate circular-interface level-set functions with evenly spaced radii from r_{\min} to r_{\max} . For each radius, we choose N_C random centers within the unit square $[-1/2, +1/2]^2 \subset \Omega$. Then, we use the resulting $\phi(\mathbf{x})$ to create the starting coarse and fine grids, \mathcal{G}_c^0 and \mathcal{G}_f^0 , with uniform bands around Γ^0 . Next, we evaluate $\phi(\mathbf{x})$ and $\mathcal{V}_i(\mathbf{x})$ on both meshes and conclude with preparatory reinitialization before interleaving advection and collecting samples. To improve the accuracy on the fine grid, we use B_c times as many redistancing operations on the nodal level-set values ϕ_f^0 as we do on the coarse-grid ϕ_c^0 . Specifically, we have selected $\nu = 10$ iterations for solving eq. (3), which is typical for many level-set applications. Besides ℓ_c^{\max} and ℓ_f^{\max} , ν is another parameter limiting the scope of $\mathcal{F}_{c,f}(\cdot)$; the reason is that one must determine ν ahead of time depending on the problem and the accuracy-performance tradeoff. Last, we launch the `IntAdvectAndCollectSamples()` procedure and accumulate the output samples into the learning data set \mathcal{D} .

We present the coarse- and fine-grid simultaneous advection subroutine to assemble \mathcal{D} in Algorithm 4. Our method follows the natural flow of a DNS on \mathcal{G}_c with interleaved updates to the level-set function on \mathcal{G}_f . In addition, it incorporates the alternating mechanism depicted in fig. 3 and periodic resetting operations for trajectory synchronization. Formal parameters to Algorithm 4 include the initial-condition level-set vectors and velocity matrices. Also, it requires the external divergence-free velocity function $\mathcal{V}(\mathbf{x})$ and the coarse- and fine-grid structural features. As before, our constraints help us define the coarse-grid time step as $\Delta t_c = h_c$ (and $\Delta t_f = h_f$), given that $\max \|\mathcal{V}(\mathbf{x})\| = 1$ for all points in Ω .

In each iteration, the main simulation loop in Algorithm 4 first advances the fine-grid level-set function from $\phi_f^n \equiv \phi_f(t_c^n)$ to $\phi_f^{n+1} \equiv \phi_f(t_c^{n+1}) \equiv \phi_f(t_c^n + \Delta t_c)$. That way, we know which reference level-set values are expected for arrival points next to the interface in \mathcal{G}_c^n during sampling. The `AdvectFineGrid()` subroutine works as a black box that retrieves the updated fine mesh and its nodal level-set values and velocities. Algorithm 5 describes the actions implied by this module. Briefly, Algorithm 5 is an iterative process based on the `SemiLagrangian()` scheme of [57]. More precisely, it transports ϕ_f^n , reinitializes the new level-set values, and reevaluates $\mathcal{V}(\mathbf{x})$ on the updated grid at regular time intervals. About redistancing on \mathcal{G}_f , it is worth emphasizing that we need $B_f \cdot \nu$ iterations in the last fine-grid advection step. The reason for them is that we want to ensure that ϕ_f^{n+1} resembles a signed distance function accurately as far as B_c coarse cells away from Γ_f .

After advecting ϕ_f^n to ϕ_f^{n+1} , we decide whether one should collect samples for the current iteration. If not, we simply call the `AdvectCoarseGrid()` module (see Algorithm 6) and retrieve the updated grid and (reinitialized)

Algorithm 3: $\mathcal{D} \leftarrow \text{GenerateDataSet}(\ell_c^{\max}, \ell_f^{\max}, t^{\text{end}}, \nu, N_F, N_C, B_c, R_{\text{freq}}, CFL)$: Generate learning data set.

Input: maximum refinement levels per unit length, ℓ_c^{\max} and ℓ_f^{\max} ; final time per configuration, t^{end} ; number of iterations for level-set redistancing, ν ; number of random velocity fields, N_F ; number of circular-interface level-set functions with the same radius per velocity field, N_C ; uniform band half-width around coarse interface, B_c ; coarse grid reset frequency, R_{freq} ; CFL number.

Result: data set with learning samples, \mathcal{D} .

```

1 define  $\Omega \equiv [-1, +1]^2 \subset \mathbb{R}^2$ , with 2 quadtrees in each Cartesian direction;
2  $B_f \leftarrow \frac{7}{4} B_c \cdot 2^{\left(\frac{\ell_f^{\max} - \ell_c^{\max} - 1}{2}\right)}$ ; // Uniform band half-width around fine grid
3  $h_c \leftarrow 2^{-\ell_c^{\max}}$ ,  $h_f \leftarrow 2^{-\ell_f^{\max}}$ ; // Coarse and fine mesh sizes
4  $r_{\min} \leftarrow 5h_c$ ,  $r_{\max} \leftarrow 0.25$ ; // Circular-interface radial bounds
5  $N_r \leftarrow \left\lceil 3 \left( \frac{r_{\max} - r_{\min}}{h_c} \right) \right\rceil + 1$ ; // Number of distinct radii
6  $\mathcal{D} \leftarrow \emptyset$ ;
   // Perform multiple simulations for  $N_F$  velocity fields
7 for  $i \leftarrow 1$  to  $N_F$  do
8    $V_i(\mathbf{x}) \leftarrow \text{GenerateVelocityField}()$ ; // Generate a random, divergence-free velocity field
9   normalize  $V_i(\mathbf{x})$ ; // and normalize it so that  $\max V_i(\mathbf{x}) = 1, \forall \mathbf{x} \in \Omega$ 
   // Evaluate  $N_r$  evenly spaced interface radii  $r \in [r_{\min}, r_{\max}]$ 
10  foreach radius  $r$  in  $\text{LinSpace}(r_{\min}, r_{\max}, N_r)$  do
   // Repeat each radius  $r$  as many as  $N_C$  times
11  for  $j \leftarrow 1$  to  $N_C$  do
12     $(x_0, y_0) \sim \mathcal{U}(-1/2, +1/2)$ ; // Random center
13     $\phi(\mathbf{x}) \leftarrow \text{LevelSet}(r, x_0, y_0)$ ; // Build circular-interface level-set function
14     $\mathcal{G}_c^0 \leftarrow \text{GenerateGrid}(\Omega, \phi(\mathbf{x}), \ell_c^{\max}, B_c)$ ; // Build initial grids
15     $\mathcal{G}_f^0 \leftarrow \text{GenerateGrid}(\Omega, \phi(\mathbf{x}), \ell_f^{\max}, B_f)$ ;
16     $\phi_c^0 \leftarrow \text{Evaluate}(\phi(\mathbf{x}), \mathcal{G}_c^0)$ ,  $U_c^0 \leftarrow \text{Evaluate}(V_i(\mathbf{x}), \mathcal{G}_c^0)$ ; // Sample level-set function
17     $\phi_f^0 \leftarrow \text{Evaluate}(\phi(\mathbf{x}), \mathcal{G}_f^0)$ ,  $U_f^0 \leftarrow \text{Evaluate}(V_i(\mathbf{x}), \mathcal{G}_f^0)$ ; // and velocity field
18     $\phi_c^0 \leftarrow \text{Reinitialize}(\mathcal{G}_c^0, \phi_c^0, \nu)$ ,  $\phi_f^0 \leftarrow \text{Reinitialize}(\mathcal{G}_f^0, \phi_f^0, B_c \cdot \nu)$ ;
   // Collect learning samples into  $\mathcal{D}_c$  (see Algorithm 4)
19     $\mathcal{D}_c \leftarrow \text{IntAdvectAndCollectSamples}(\mathcal{G}_c^0, \mathcal{G}_f^0, \phi_c^0, \phi_f^0, U_c^0, U_f^0, t^{\text{end}}, \nu, V_i(\mathbf{x}), B_c, B_f, h_c, h_f, R_{\text{freq}}, CFL)$ ;
20     $\mathcal{D} \leftarrow \mathcal{D} \cup \mathcal{D}_c$ ;
21  end
22 end
23 end
24 return  $\mathcal{D}$ ;

```

nodal level-set values into \mathcal{G}_c^{n+1} and ϕ_c^{n+1} . The `AdvectCoarseGrid()` subroutine is equivalent to a single step in Algorithm 5 performed on \mathcal{G}_c with an additional reset operation. We will provide more details and the justification for the `FitToFineGrid()` reset statement below as we dive into data sampling.

In the case of a data-collection iteration, we start by computing coarse-grid nodal curvature values, normal unit vectors, and level-set second-order derivatives. Then, we fetch training input data through the `CollectDataPackets()` procedure listed in Algorithm 2. The sampling portion in `IntAdvectAndCollectSamples()` replicates the first group of statements in our `MLSemiLagrangian()` algorithm. However, instead of constructing a batch of pre-processed entries, we accumulate learning tuples using the data packets in \mathcal{D} as inputs. We denote a learning tuple by

$$\xi \doteq (\rho, \tilde{\phi}_d^*) \in \mathbb{R}^{23}, \quad (18)$$

where ρ is the blob shown in eq. (14), and $\tilde{\phi}_d^*$ is the h_c -normalized reference level-set value at the departure point. To calculate $\tilde{\phi}_d^*$, we turn to quadratic interpolation from ϕ_f^{n+1} . This strategy leverages ϕ_f^{n+1} 's higher accuracy and the fact that the coarse-grid vertices around Γ_c^n are a proper subset of the fine-mesh uniform band around $\Gamma_f^{n+1} \equiv \Gamma_f^n + \Delta t_c$. Similar to Algorithm 1, we reorient $\rho \in \xi$ into its standard form and apply negative-curvature normalization. At the

Algorithm 4: $\mathcal{D}_c \leftarrow \text{IntAdvectAndCollectSamples}(\mathcal{G}_c^0, \mathcal{G}_f^0, \phi_c^0, \phi_f^0, U_c^0, U_f^0, t^{end}, v, V(\mathbf{x}), B_c, B_f, h_c, h_f, R_{freq}, CFL)$: Interleave advection of coarse and fine grids while collecting learning samples.

Input: initial coarse grid and its level-set values and velocities, $\mathcal{G}_c^0, \phi_c^0$, and U_c^0 ; initial fine grid and its nodal level-set values and velocities, $\mathcal{G}_f^0, \phi_f^0$, and U_f^0 ; final advection time, t^{end} ; number of iterations for level-set redistancing, v ; velocity field, $V(\mathbf{x})$; uniform band half-width around coarse interface, B_c ; uniform band half-width around fine interface, B_f ; coarse mesh size, h_c ; fine mesh size, h_f ; coarse-grid reset frequency, R_{freq} ; CFL number.

Result: coarse-grid learning data set, \mathcal{D}_c .

```

1  $t_c^n \leftarrow 0, \quad \Delta t_c \leftarrow CFL \cdot h_c / \max \|V(\mathbf{x})\|, \quad iter \leftarrow 0; \quad //$  Coarse grid stepping variables
2  $(\mathcal{G}_c^n, \phi_c^n, U_c^n) \leftarrow (\mathcal{G}_c^0, \phi_c^0, U_c^0), \quad (\mathcal{G}_f^n, \phi_f^n, U_f^n) \leftarrow (\mathcal{G}_f^0, \phi_f^0, U_f^0);$ 
3  $\mathcal{D}_c \leftarrow \emptyset;$ 
   // Interleave advection of  $\phi_c$  and  $\phi_f$  using their respective structures in  $\mathcal{G}_c$  and  $\mathcal{G}_f$ 
4 while  $t_c^n < t^{end}$  do
5   adjust  $\Delta t_c$  if  $t_c^n + \Delta t_c > t^{end}$ ;
6    $(\mathcal{G}_f^{n+1}, \phi_f^{n+1}, U_f^{n+1}) \leftarrow \text{AdvectFineGrid}(\mathcal{G}_f^n, \phi_f^n, U_f^n, t_c^n, t_c^n + \Delta t_c, v, V(\mathbf{x}), B_c, B_f, h_f, CFL);$  // See Algorithm 5
   // Alternating between sampling and standard advection
7   if 2 divides  $iter$  evenly then
8      $(\kappa_c^n, N_c^n) \leftarrow \text{ComputeCurvatureAndNormal}(\mathcal{G}_c^n, \phi_c^n);$  // Nodal curvature and normal unit vectors
9      $\Phi_{c,xx}^n \leftarrow \text{SecondSpatialDerivatives}(\mathcal{G}_c^n, \phi_c^n);$  //  $\phi_{xx}$  and  $\phi_{yy}$  at the nodes of  $\mathcal{G}_c^n$ 
10     $\mathcal{H}_f^{n+1} \leftarrow \text{Reconstruct}(\mathcal{G}_f^{n+1}), \quad \mathcal{H}_c^n \leftarrow \text{Reconstruct}(\mathcal{G}_c^n);$  // Fine and coarse tree hierarchies
   // Collect and process data packets to create learning samples
11    $(\mathcal{P}, \mathcal{C}) \leftarrow \text{CollectDataPackets}(\mathcal{G}_c^n, \mathcal{H}_c^n, \phi_c^n, U_c^n, \Phi_{c,xx}^n, N_c^n, \kappa_c^n, \Delta t_c);$  // See Algorithm 2
12    $M_\phi \leftarrow \emptyset;$  // Map from node coordinates to  $\phi$  values interpolated from  $\phi_f^{n+1}$ 
13   foreach data packet  $p \in \mathcal{P}$  do
14     let  $\mathbf{x}_a$  be the coordinates (i.e., arrival point) corresponding to  $p$  in  $\mathcal{C}$ ;
15      $\tilde{\phi}_d^* \leftarrow \text{Interpolate}(\mathcal{H}_f^{n+1}, \phi_f^{n+1}, \mathbf{x}_a) / h_c;$  // Use advected fine grid to get normalized  $\phi_d^*$ 
16     let  $\xi$  be the learning tuple  $(p, \tilde{\phi}_d^*)$  with inputs  $p$  and expected output  $\tilde{\phi}_d^*$ ;
17     transform  $\xi$ , so that  $p \cdot \kappa_a$  is negative;
18     rotate  $\xi$ , so that the angle of  $-p \cdot \hat{\mathbf{u}}_a$  lies between 0 and  $\pi/2$ ;
19     add tuple  $\xi$  to  $\mathcal{D}_c$ ;
20     let  $\xi'$  be the reflected tuple about line  $y = x + \beta$  going through  $\mathbf{x}_a$ ; // Data augmentation
21     add  $\xi'$  to  $\mathcal{D}_c$ ;
22      $M_\phi[\mathbf{x}_a] \leftarrow h_c \tilde{\phi}_d^*;$  // Caching expected or improved level-set values
23   end
24   if  $R_{freq}$  divides  $(iter + 1)$  evenly then
25      $(\mathcal{G}_c^{n+1}, \phi_c^{n+1}) \leftarrow \text{FitToFineGrid}(\mathcal{G}_c^n, \phi_c^n, \mathcal{G}_f^{n+1}, \phi_f^{n+1});$  // Reset coarse grid
26   else
27      $(\mathcal{G}_c^{n+1}, \phi_c^{n+1}) \leftarrow \text{SemiLagrangian}(\mathcal{G}_c^n, \phi_c^n, U_c^n, U_c^n, CFL);$  // Refer to Algorithm 3 in [57]
28     AdjustLevelSetWithMLSolution( $\phi_c^{n+1}, M_\phi$ ); // Correct  $\phi_c^{n+1}$  for nodes with coords in  $M_\phi$ 
29   end
30    $\mathcal{W} \leftarrow \text{GetCoordsWithNegativeFlow}(\mathcal{H}_c^n, U_c^n, N_c^n, \mathcal{G}_c^{n+1}, \phi_c^{n+1});$  // Points 'lagging behind'  $\Gamma_c^{n+1}$ 
31    $\phi_c^{n+1} \leftarrow \text{SelectiveReinitialization}(\mathcal{G}_c^{n+1}, \phi_c^{n+1}, \mathcal{C} \cap \mathcal{W}, v);$ 
32 else
33    $(\mathcal{G}_c^{n+1}, \phi_c^{n+1}) \leftarrow \text{AdvectCoarseGrid}(\mathcal{G}_c^n, \phi_c^n, U_c^n, \mathcal{G}_f^{n+1}, \phi_f^{n+1}, v, iter, R_{freq}, CFL);$  // See Algorithm 6
34 end
35    $U_c^{n+1} \leftarrow \text{Evaluate}(V(\mathbf{x}), \mathcal{G}_c^{n+1});$  // Resample velocity field
36    $iter \leftarrow iter + 1, \quad t_c^n \leftarrow t_c^n + \Delta t_c;$  // and update stepping variables
37    $(\mathcal{G}_c^n, \phi_c^n, U_c^n) \leftarrow (\mathcal{G}_c^{n+1}, \phi_c^{n+1}, U_c^{n+1}), \quad (\mathcal{G}_f^n, \phi_f^n, U_f^n) \leftarrow (\mathcal{G}_f^{n+1}, \phi_f^{n+1}, U_f^{n+1});$ 
38 end
39 return  $\mathcal{D}_c$ ;

```

Algorithm 5: $(\mathcal{G}_f^F, \phi_f^F, U_f^F) \leftarrow \text{AdvectFineGrid}(\mathcal{G}_f^0, \phi_f^0, U_f^0, t_f^0, t_f^F, \nu, \mathcal{V}(\mathbf{x}), B_c, B_f, h_f, CFL)$: Advect fine-grid level-set values from ϕ_f^0 to ϕ_f^F and update nodal velocities.

Input: fine grid and its nodal level-set values and velocities, $\mathcal{G}_f^0, \phi_f^0$, and U_f^0 ; initial advection time, t_f^0 ; ending advection time, t_f^F ; number of iterations for level-set redistancing, ν ; velocity field, $\mathcal{V}(\mathbf{x})$; uniform band half-width around coarse interface, B_c ; uniform band half-width around fine interface, B_f ; mesh size, h_f ; CFL number.

Result: updated fine grid structure, \mathcal{G}_f^F , nodal level-set values, ϕ_f^F , and nodal velocities, U_f^F , at time t_f^F .

```

1  $t_f^n \leftarrow t_f^0, \quad \Delta t_f \leftarrow CFL \cdot h_f / \max \|\mathcal{V}(\mathbf{x})\|; \quad // \text{Stepping variables}$ 
2  $(\mathcal{G}_f^n, \phi_f^n, U_f^n) \leftarrow (\mathcal{G}_f^0, \phi_f^0, U_f^0);$ 
3 while  $t_f^n < T$  do
4     adjust  $\Delta t_f$  if  $t_f^n + \Delta t_f > t_f^F$ ;
5      $(\mathcal{G}_f^{n+1}, \phi_f^{n+1}) \leftarrow \text{SemiLagrangian}(\mathcal{G}_f^n, \phi_f^n, U_f^n, U_f^n, CFL); \quad // \text{Refer to Algorithm 3 in [57]}$ 
6     if  $t_f^n + \Delta t_f < t_f^F$  then
7          $\phi_f^{n+1} \leftarrow \text{Reinitialize}(\mathcal{G}_f^{n+1}, \phi_f^{n+1}, B_c \cdot \nu);$ 
8     else
9          $\phi_f^{n+1} \leftarrow \text{Reinitialize}(\mathcal{G}_f^{n+1}, \phi_f^{n+1}, B_f \cdot \nu); \quad // \text{Increase redistancing accuracy in last step}$ 
10    end
11     $U_f^{n+1} \leftarrow \text{Evaluate}(\mathcal{V}(\mathbf{x}), \mathcal{G}_f^{n+1}); \quad // \text{Resample velocity field}$ 
12     $t_f^n \leftarrow t_f^n + \Delta t_f;$ 
13     $(\mathcal{G}_f^n, \phi_f^n, U_f^n) \leftarrow (\mathcal{G}_f^{n+1}, \phi_f^{n+1}, U_f^{n+1});$ 
14 end
15  $(\mathcal{G}_f^F, \phi_f^F, U_f^F) \leftarrow (\mathcal{G}_f^n, \phi_f^n, U_f^n);$ 
16 return  $(\mathcal{G}_f^F, \phi_f^F, U_f^F);$ 

```

same time, we store ϕ_d^* for next-to- Γ_c^n nodes in a cache, \mathcal{M}_ϕ . Later, we will merge these target values with the rest of the elements in ϕ_c^{n+1} advected numerically.

Besides accumulating reoriented-input samples, as in fig. 5b, we also exploit symmetry and invariance in data packet fields to supplement \mathcal{D} with augmented pairs. Data augmentation via rotations and reflections has proven effective for image classifiers with convolutional networks [1, 3]. Here, we augment samples by reflecting $p \in \xi$ about the line $y = x + \beta$ going through the origin of the local coordinate system centered at p 's arrival point (see fig. 5c).

Next, we advance the coarse-grid level-set values after collecting learning samples for time t^n into the cumulative set \mathcal{D}_c . To evolve ϕ_c^n to ϕ_c^{n+1} and update \mathcal{G}_c^n , we could have only called the `SemiLagrangian()` procedure and merged the reference ϕ_d^* values from \mathcal{M}_ϕ back into ϕ_c^{n+1} . However, the discretized coarse- and fine-mesh level-set functions can diverge to the point where our numerical-error characterization with $\mathcal{F}_{c,f}(\cdot)$ becomes invalid. Therefore, we reset ϕ_c^{n+1} periodically through the `FitToFineGrid()` method by interpolating its level-set values from ϕ_f^{n+1} every $R_{freq} = 3$ iterations. This recurrent synchronization protects against large trajectory deviations while preserving the natural noise that emerges from ϕ_c^n 's conventional advection.

The last steps in Algorithm 4's sampling iteration involve reinitializing ϕ_c^{n+1} . Such a task is subtle and requires special care in our machine learning strategy. In particular, we should solve eq. (3) *just* for values in ϕ_c^{n+1} that we did not update via interpolation from ϕ_f^{n+1} and for which the condition in eq. (17) is not satisfied. Thus, one must use selective reinitialization to guard the machine-learning-corrected values with the help of the auxiliary arrays \mathcal{C} and \mathcal{W} . As shown in Section 6, the `SelectiveReinitialization()` and `MLSemiLagrangian()` subroutines work together with alternating transport transport to ensure that the moving front remains smooth and as close as possible to a higher-resolution counterpart.

The purpose of Algorithm 4 is to accumulate learning samples in a local set until we reach the final simulation time. Then, upon exiting `IntAdvectAndCollectSamples()`, we return to the `GenerateDataSet()` function, where \mathcal{D} appends the partial results arriving from every DNS configuration. By the end of Algorithm 3, \mathcal{D} contains all the tuples in the form given by eq. (18). In the following tasks, we employ this data set to train and assess $\mathcal{F}_{c,f}(\cdot)$.

5.4.2. Technical aspects

Training an error-correcting neural network is much more resource-intensive than constructing its learning data set. Even though assembling \mathcal{D} is algorithmically complex and can take several hours, one must perform this task just once

Algorithm 6: $(\mathcal{G}_c^{n+1}, \phi_c^{n+1}) \leftarrow \text{AdvectCoarseGrid}(\mathcal{G}_c^n, \phi_c^n, U_c^n, \mathcal{G}_f^{n+1}, \phi_f^{n+1}, \nu, \text{iter}, R_{freq}, CFL)$: Advect coarse-grid level-set values from ϕ_c^n to ϕ_c^{n+1} and perform reinitialization.

Input: coarse grid and its nodal level-set values and velocities, $\mathcal{G}_c^n, \phi_c^n$, and U_c^n ; updated fine grid and its nodal level-set values, \mathcal{G}_f^{n+1} and ϕ_f^{n+1} ; number of iterations for level-set redistancing, ν ; current simulation iteration, iter ; coarse-grid reset frequency, R_{freq} ; CFL number.

Result: updated coarse grid structure, \mathcal{G}_c^{n+1} , and reinitialized nodal level-set values, ϕ_c^{n+1} .

```

1 if  $R_{freq}$  divides  $(\text{iter} + 1)$  evenly then
2   |  $(\mathcal{G}_c^{n+1}, \phi_c^{n+1}) \leftarrow \text{FitToFineGrid}(\mathcal{G}_c^n, \phi_c^n, \mathcal{G}_f^{n+1}, \phi_f^{n+1});$            // Reset coarse grid
3 else
4   |  $(\mathcal{G}_c^{n+1}, \phi_c^{n+1}) \leftarrow \text{SemiLagrangian}(\mathcal{G}_c^n, \phi_c^n, U_c^n, U_c^n, CFL);$            // Refer to Algorithm 3 in [57]
5 end

6  $\phi_c^{n+1} \leftarrow \text{Reinitialize}(\mathcal{G}_c^{n+1}, \phi_c^{n+1}, \nu);$ 
7 return  $(\mathcal{G}_c^{n+1}, \phi_c^{n+1});$ 

```

at the beginning of the learning stage. Optimizing $\mathcal{F}_{c,f}(\cdot)$, on the contrary, is less cumbersome but requires exploring an extensive hyperparameter space through multiple evaluations. Every such trial can last many hours depending on $|\mathcal{D}|$ and the size of the hidden layers in $\mathcal{F}_{c,f}(\cdot)$.

In this work, we realize Algorithms 1 to 6 with our in-house, C++ implementation of the parallel level-set framework of [57]. As for learning, we simplify most of the tasks with the help of the building blocks provided by TensorFlow [82] and Keras [83] in Python. In addition, we follow conventional practices [1, 2] and split \mathcal{D} into non-overlapping training, testing, and validation subsets to optimize $\mathcal{F}_{c,f}(\cdot)$ and promote generalization. Our partitioning approach also ensures that each subset mirrors the output $\tilde{\phi}_d^*$ distribution in \mathcal{D} . The specific heuristics that make this possible rely on the `StratifiedKFold()` method from the SciKit-Learn library [84]. Although scientists usually reserve this balancing subroutine for classification problems, we have introduced it to our regression setup by employing Pandas' `cut()` procedure [85]. The `cut()` function first allows us to bin the reference level-set values into discrete intervals. Then, we call `StratifiedKFold()` three times with $K = 10$ to populate the training, testing, and validation subsets with 70%, 10%, and 10% of the tuples in \mathcal{D} . The remaining 10% is discarded as a way of performing balanced subsampling. However, we do not carry out the expensive, full-fledged 10-fold cross-validation during hyperparameter tuning. We have observed that a single fold with a couple of random initializations is sufficient, given that \mathcal{D} is large.

The other critical component in our machine-learning extension to semi-Lagrangian schemes is the `Preprocess()` module portrayed in figs. 3 and 4. The `Preprocess()` actions depend on training subset statistics and help transform raw feature vectors into amenable representations for the numerical error estimator [84]. In our hyperparameter space exploration, we have discovered the existence of three types of preprocessing operations that favor convergence, speed, and precision. Algorithm 7 lists these preprocessing adjustments performed on data-packet attributes before assembling input vectors for $\mathcal{F}_{c,f}(\cdot)$ (see eq. (16)). First, we h -scale the distance-related data in p (e.g., departure-arrival-point distance, level-set values, level-set second-order derivatives, and curvature). Then, we use the feature-type-based statistics \mathcal{Q} extracted from the training subset to perform data (quasi) standardization. The latter comprises centering and scaling p entries using the mean and standard deviation calculated *across* features of the same kind. For example, the `Standardize()` method in Algorithm 7 replaces $\varphi \in \Psi \subset p$ for $(\varphi - \mathcal{Q}.\mu_\varphi)/\mathcal{Q}.\sigma_\varphi$, where $\mathcal{Q}.\mu_\varphi$ and $\mathcal{Q}.\sigma_\varphi$ are the level-set mean and standard deviation computed across $\Psi \doteq \{\phi_a, (\phi_d)_{ij}, \phi_d\}$, with $i, j \in \{0, 1\}$.

In the last group of preprocessing operations, we use principal component analysis (PCA) and whitening alongside dimensionality reduction. PCA and whitening are well known for accelerating convergence, and practitioners have shown that their combination leads to better results than ordinary z-scoring [46, 86]. Coupling standardization and PCA is also beneficial because it prevents variance from directly reflecting the scale of the data [79]. As for whitening, we have incorporated it because it adds a secondary per-component scaling layer that raises uncorrelated concepts to the same level of importance (on an a priori basis) [1]. In our case, we employ SciKit-Learn's PCA class to transform standardized data packets into input vectors with $\mathcal{Q}.N_{comp} = 17$ entries. After settling down with an optimal model, we export $\mathcal{F}_{c,f}(\cdot)$, \mathcal{Q} , and the PCA object to JSON files. Then, we can use these files for porting the entire inference system in fig. 4 to various platforms.

We close this section by providing some insight into training $\mathcal{F}_{c,f}(\cdot)$ with TensorFlow and Keras. As seen in fig. 4, our multilayer perceptron has $17 + 1$ linear input neurons that ingest data coming from the `Preprocess()` module and $\tilde{\phi}_d$ at the departure point. The first four hidden layers contain N_h^i nonlinear, ReLU units, for $i = 1, 2, 3, 4$, with

Algorithm 7: $\mathbf{p} \leftarrow \text{Preprocess}(p, h)$: Preprocess a data packet p using training statistics.

Input: data packet to preprocess, p ; mesh size, h .
Result: preprocessed data packet as a vector \mathbf{p} .

```

// In-place  $h$ -scaling groups of variables in  $p$ 
1 Divide  $p.\phi_a$ ,  $p.(\phi_d)_{ij}$ , and  $p.\phi_d$  by  $h$ ; // Take  $i, j \in \{0, 1\}$ 
2 Multiply  $p.\phi_{xx}$  and  $p.\phi_{yy}$  by  $h^2$ ;
3 Multiply  $p.\kappa_a$  by  $h$ ;
4 Divide  $p.d$  by  $h$ ;

// In-place (quasi) standardization
5  $\mathcal{Q} \leftarrow \text{GetStats}()$ ; // Retrieve training stats
6 Standardize( $[p.\phi_a, p.(\phi_d)_{ij}, p.\phi_d]$ ,  $\mathcal{Q}.\mu_\phi$ ,  $\mathcal{Q}.\sigma_\phi$ );
7 Standardize( $[p.\mathbf{u}_a, p.(\mathbf{u}_d)_{ij}]$ ,  $\mathcal{Q}.\mu_{\mathbf{u}}$ ,  $\mathcal{Q}.\sigma_{\mathbf{u}}$ );
8 Standardize( $[p.d]$ ,  $\mathcal{Q}.\mu_d$ ,  $\mathcal{Q}.\sigma_d$ );
9 Standardize( $[p.\tilde{x}_d, p.\tilde{y}_d]$ ,  $\mathcal{Q}.\mu_{\text{coords}}$ ,  $\mathcal{Q}.\sigma_{\text{coords}}$ );
10 Standardize( $[p.(\phi_{xx})_d, p.(\phi_{yy})_d]$ ,  $\mathcal{Q}.\mu_{\text{xyy}}$ ,  $\mathcal{Q}.\sigma_{\text{xyy}}$ );
11 Standardize( $[p.\kappa]$ ,  $\mathcal{Q}.\mu_\kappa$ ,  $\mathcal{Q}.\sigma_\kappa$ );

// Dimensionality reduction and whitening
12  $\mathbf{p} \leftarrow \text{PCA}(p, \mathcal{Q}.N_{\text{comp}})$ ; // PCA and whitening with  $N_{\text{comp}}$  components
13 return  $\mathbf{p}$ ;
```

trainable connections and parameters. The last hidden-layer neuron is linear and updatable, and the output unit merely adds its input tensors requiring no trainable weights. To train $\mathcal{F}_{c,f}(\cdot)$, we have used backpropagation with the Adam optimizer to minimize the root mean squared error loss (RMSE) between $\tilde{\phi}_d^*$ and $\tilde{\varepsilon} + \tilde{\phi}_d$. Besides this typical loss, we have introduced kernel regularizers in all hidden layers with an L2 regularization factor of 10^{-6} . Weight updates take place after evaluating the RMSE over batches with 64 samples. In addition, we monitor the mean absolute error (MAE) on the validation subset to reduce the learning rate systematically and prevent overfitting. In particular, we stabilize optimization by attaching a callback function that halves the learning rate from 1.5×10^{-4} down to 1.5×10^{-5} whenever the validation MAE does not improve for fifteen epochs. Also, we stop backpropagation as a protective measure if the latter MAE continues to deteriorate for fifty iterations. In any case, we have observed that a maximum of one thousand iterations suffices for training $\mathcal{F}_{c,f}(\cdot)$. Thanks to Keras' facilities and callback methods, we can easily handle these and other technical aspects, like best-model checkpoints and logging. The upcoming section confirms this complete process by producing an error-correcting neural network for a pair of c and f grid resolutions.

6. Results

Now, we assess the feasibility of the ideas presented in Section 5. Our proof of concept comprises a neural model, $\mathcal{F}_{6,8}(\cdot)$, designed for a relatively coarse grid composed of unit-square quadtrees with $\ell_c^{\max} = 6$. As for the fine grid that supplies the reference level-set values, ϕ_d^* , we require $\ell_f^{\max} = 8$ and $h_f = 2^{-8}$. Consequently, our error-correcting neural network, the `MLSemiLagrangian()` subroutine with selective reinitialization, and the numerical `SemiLagrangian()` scheme must operate in tandem to improve the interface advection accuracy over a discretization with $h_c = 2^{-6} = 0.015625$.

To optimize $\mathcal{F}_{6,8}(\cdot)$, we gathered 4'051,946 samples from the methodologies outlined in Algorithms 2 to 6. Then, we used stratified K -fold indexing (see Section 5.4.2) to discard about 10% of them and allocate 2'836,283, 405,203, and 405,213 tuples for the training, testing, and validation subsets. Hence, our curated learning set, \mathcal{D}' , ended up with 3'646,699 samples. Exploring the hyperparameter space with \mathcal{D}' resulted in an optimal architecture with $N_h^i = 130$ units in the first four hidden layers. The topology in fig. 4 thus gave rise to 53,561 parameters that we trained during 337 epochs. At this stage, we also discovered that reducing input vectors from 22 to 17 dimensions was critical for learning stability and accuracy. While fewer than 17 components in the PCA object led to underfitting, more than these did not translate into any significant improvements. Likewise, employing over 17 dimensions precipitated outliers' appearance because of the additional whitening normalization. This problem is not new, and we have reported it when computing curvature in [46].

Figure 7 contrasts the fitting quality of the numerical baseline and $\mathcal{F}_{6,8}(\cdot)$ over the entire learning data set. These results confirm that the error-correcting function aids in closing the gap between the estimated and the reference level-

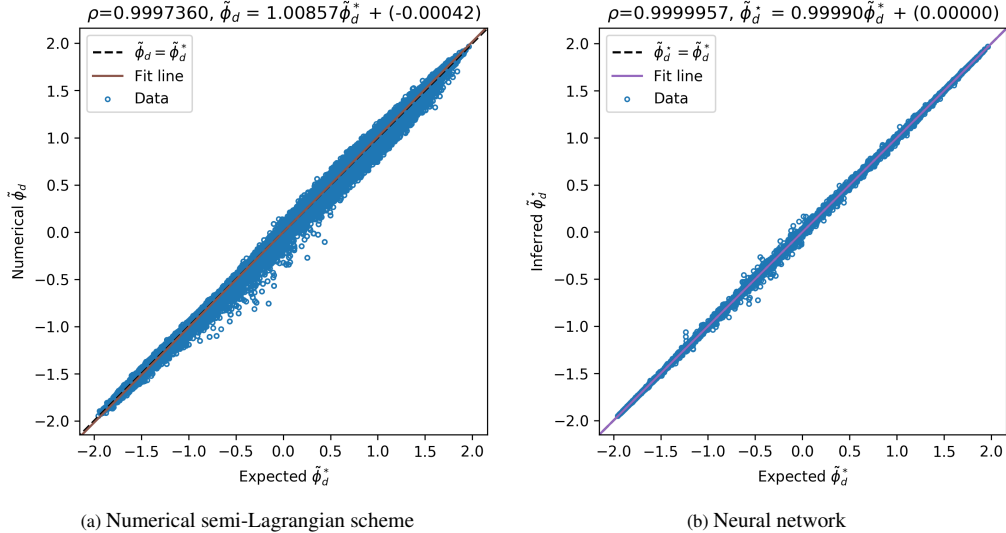


Figure 7: Learning output correlation plots over \mathcal{D}' between expected and approximated h_c -normalized level-set values at the departure points. (Color online.)

	MAE	ℓ^∞ error	RMSE
Neural network	7.990813×10^{-4}	2.535921×10^{-1}	1.744662×10^{-3}
Numerical semi-Lagrangian scheme	9.113001×10^{-3}	6.033318×10^{-1}	1.471008×10^{-2}

Table 1: Learning output statistics over \mathcal{D}' for h_c -normalized level-set values at the departure points.

set values during semi-Lagrangian advection. Table 1 supports this observation. Our neural network helps reduce the MAE by 91% and lowers the maximum error by a factor of 2.4 in \mathcal{D}' . These figures ratify that the conventional scheme in eqs. (6) to (8) can benefit from data-driven corrections even though we cannot represent $\bar{\varepsilon}$ exactly. The following classic tests verify these benefits by showing how $\mathcal{F}_{6,8}(\cdot)$ contributes to offsetting numerical dissipation and decreasing artificial mass loss. The experiments include rotating and deforming a circle under the effect of divergence-free velocity fields and solving a couple of instances of the Stefan problem. For compatibility with $\mathcal{F}_{6,8}(\cdot)$, we have discretized Ω using quadtree Cartesian grids with unit-square macrocells and $\ell_c^{\max} = 6$ (i.e., $h_c = 2^{-6}$). Also, we ensure the simulations meet the conditions in fig. 5 by enforcing $CFL = 1$ and scaling velocity fields to fit within the unit ball (i.e., $\Delta t = h_c$) whenever possible. For consistency, we reinitialize $\phi(\mathbf{x})$ every time step using ten iterations as noted in Section 5.4.1.

We close this preamble with a remark about the hybrid inference system’s technical implementation. In the following, we have turned to Lohmann’s json suite [87] and some utilities from Hermann’s frugally-deep library [88] to import $\mathcal{F}_{6,8}(\cdot)$ and the `Preprocess()` dependencies into C++. `frugally-deep` provides a user-friendly interface for neural forward evaluations; however, we have reconstructed the internal mechanisms in $\mathcal{F}_{6,8}(\cdot)$ as a collection of weight matrices in OpenBLAS [89]. Compared with `frugally-deep`, OpenBLAS offers up to sixty times faster inference (with compiler optimization⁷) but requires arranging inputs in a specific form. To accommodate OpenBLAS constraints, we have first clustered data into batches. Then, we carried out predictions in Algorithm 1 (line 14) with one 32-bit `sgemm`⁸ operation per simulation step. In particular, this lower-precision function has not affected our system’s accuracy since $\mathcal{F}_{6,8}(\cdot)$ learned from \mathcal{D}' with the default single-floating-point TensorFlow configuration. Lastly, each of the coming assays has run in a computer with 16GB RAM, 2.2GHz processor frequency, and no multi-threading. The reported wall times correspond to the shortest durations out of ten repetitions for every experiment. We have made available $\mathcal{F}_{6,8}(\cdot)$ and related objects used in this section at <https://github.com/UCSB-CASL/ECNet>.

⁷We used the flags `-O2 -O3 -march=native` for C++11

⁸single-precision, general matrix-matrix multiplication: $C = \alpha AB + \beta C$.

Method	ℓ_c^{\max}	MAE	ℓ^∞ error	Disk area	Area loss (%)	Time (sec.)
Ours	6	4.672×10^{-4}	9.317×10^{-4}	7.027×10^{-2}	0.59	3.874
Numerical	6	3.380×10^{-3}	4.481×10^{-3}	6.740×10^{-2}	4.65	3.578
	7	8.545×10^{-4}	1.195×10^{-3}	6.985×10^{-2}	1.18	13.665
	8	2.152×10^{-4}	3.083×10^{-4}	7.048×10^{-2}	0.30	53.956

Table 2: Rotation accuracy and performance assessment. Reported errors include measurements taken at grid points for which $|\phi_{rot}(\mathbf{x})| \leq \sqrt{2}h_c$ at the end of one revolution.

6.1. Rotation

Let $\phi_{rot}(\mathbf{x})$ be a starting level-set function with a circular interface of radius $r = 0.15$ centered at $(0, 0.75)$ within $\Omega \equiv [-1, +1]^2$. If one considers the divergence-free velocity field

$$\mathbf{u}_{rot}(\mathbf{x}) = \begin{pmatrix} u(x, y) \\ v(x, y) \end{pmatrix} = \frac{1}{\sqrt{2}} \begin{pmatrix} -y \\ x \end{pmatrix}, \quad (19)$$

the disk completes one revolution at $t^{end} = 2\pi\sqrt{2}$ since $\max \|\mathbf{u}_{rot}(\mathbf{x})\| = 1, \forall \mathbf{x} \in \Omega$. Table 2 shows our hybrid strategy’s performance and the error for the interface location. In addition, it includes results for the baseline semi-Lagrangian scheme of [57] at various resolutions. Note that our approach comprises not only the `MLSemiLagrangian()` module but also a custom selective reinitialization. Like interleaved advection in Algorithm 4, selective redistancing is in place to protect a subset of the machine-learning-corrected level-set values when solving eq. (3). Furthermore, we alternate between the numerical scheme and the `MLSemiLagrangian()` subroutine to regularize the neurally inferred trajectory, as seen in fig. 3.

Compared with the baseline at $\ell_c^{\max} = 6$, the statistics in table 2 prove that $\mathcal{F}_{6,8}(\cdot)$ helps counteract numerical diffusion. In particular, the average error reduces by a factor of 7.2, and the maximum error drops around 79%. Also important is the fact that artificial area loss decreases from 4.65% to 0.59%. These low-cost benefits are made possible thanks to compiling optimization and OpenBLAS. Further, table 2 reveals that our alternating approach outperforms the numerical solver at twice the resolution. For instance, the hybrid system preserves area more accurately than the baseline at $\ell_c^{\max} = 7$ but requires less than one-third of the computation time. For completeness, the last row of table 2 includes the results for the semi-Lagrangian scheme at the reference training resolution (i.e., $\ell_c^{\max} = 8$). If one contrasts those measurements with ours, it is easy to see that the conventional method delivers smaller ℓ^1 and ℓ^∞ error norms, as expected. This behavior echoes the findings of Zhuang et al. in [64], where an advecting neural model trained on a reference grid at $8\times$ the resolution achieved roughly the same accuracy as the baseline at $4\times$ the resolution. Figure 8 offers a visual perspective to our results corresponding to five and ten full revolutions. For comparison, we also include the standard solution for $\ell_c^{\max} = 7$.

We conclude this experiment with a stress test. We compare the accuracy of our approach with the ordinary semi-Lagrangian scheme at the same ($\ell_c^{\max} = 6$) and twice the grid resolution ($\ell_c^{\max} = 7$). This time, the simulation lasts up to twenty revolutions. The resulting statistics appear in fig. 9.

Figure 9 confirms that the machine-learning-augmented semi-Lagrangian advection is superior to the baseline scheme at a compatible grid discretization with $h_c = 2^{-6}$. Here, the corrected trajectory remains close to the analytical solution, whereas the numerical interface vanishes right after the fifteenth revolution. Our strategy also outperforms the numerical accuracy at twice the resolution. Specifically, $\mathcal{F}_{6,8}(\cdot)$ helped reduce area loss by a factor of 2.6 by the end of the twentieth rotation. The latter validates that our hybrid framework minimizes the effects of unwelcome diffusion on a comparable level with a conventional solver in a discretized domain with $h_c = 2^{-7}$. Once more, these machine learning benefits come at a fraction of the cost required to solve the same problem in a mesh with eight-level unit-square quadtrees. Figure 10 closes this case study with zero-isocontour illustrations at the end of the fifteenth revolution for the three tested systems. Finally, figs. 9 and 10 clearly verify that our approach remains stable for all simulation times, independently from the chosen $t^{end} = 0.5$ in Algorithm 3. However, as seen in fig. 10b, bias artifacts can emerge as $t^n \rightarrow \infty$. In order to tackle this phenomenon, we plan on either enforcing physical constraints, introducing temporal information during training, or considering a different numerical transport method.

6.2. Vortex

Next, we consider the more challenging vortex deformation flow proposed by [90]. Let $\phi_{vtx}(\mathbf{x})$ be an initial level-set function with a circular interface of radius $r = 0.15$ centered at $(0.5, 0.75)$ within $\Omega \equiv [0, 1]^2$. If we define the

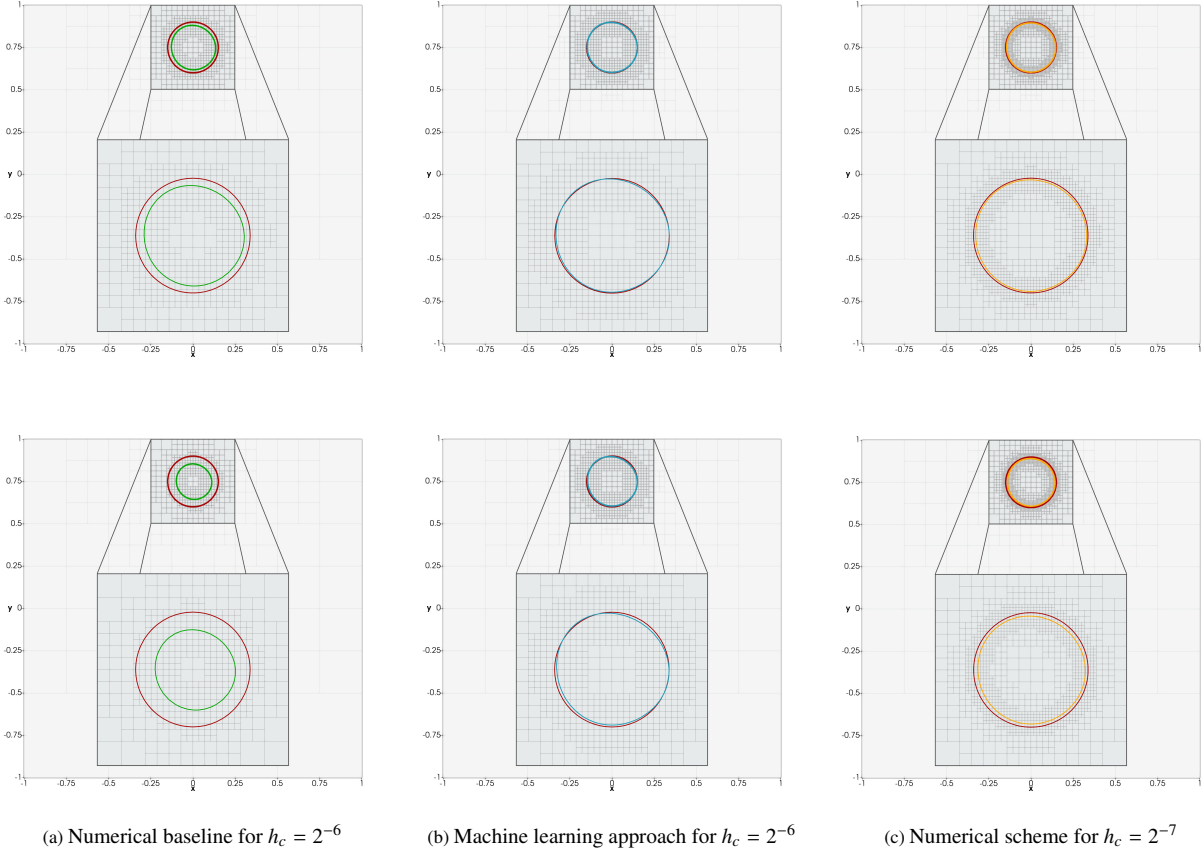


Figure 8: Rotation problem zero level sets at the end of five (i.e., $t^{end} = 10\pi\sqrt{2}$) (top row) and ten (i.e., $t^{end} = 20\pi\sqrt{2}$) (bottom row) revolutions. Left and right columns show the numerical scheme in green and orange for $\ell_c^{\max} = 6, 7$. The center column provides the machine-learning-corrected solution in blue for $\ell_c^{\max} = 6$. In all cases, the analytical disk appears in red. (Color online.)

divergence-free velocity field

$$\mathbf{u}_{vtx}(\mathbf{x}) = \begin{pmatrix} u(x, y) \\ v(x, y) \end{pmatrix} = \begin{pmatrix} -\sin^2(\pi x) \sin(2\pi y) \\ \sin^2(\pi y) \sin(2\pi x) \end{pmatrix}, \quad (20)$$

the circle deforms into a (clockwise) spiral with $\max \|\mathbf{u}_{vtx}(\mathbf{x})\| = 1$, $\forall \mathbf{x} \in \Omega$. In this experiment, we evolve the starting interface forward with eq. (20) until $t^{mid} = 0.625$ and then backward using $-\mathbf{u}_{vtx}(\mathbf{x})$. The goal is to examine how accurately we can reconstruct the original disk at time $t^{end} = 1.25$.

Table 3 summarizes the interface location accuracy and performance metrics for this experiment on several mesh discretizations. According to these statistics, our method is superior to the numerical baseline at $\ell_c^{\max} = 6$ but is not as good as the conventional semi-Lagrangian advection at twice the resolution (at least in terms of the MAE). In particular, $\mathcal{F}_{6,8}(\cdot)$ helps reduce the ℓ^1 error norm by 30%, the maximum error by one third, and the area loss by 83% when $h_c = 2^{-6}$. Figure 11 confirms these findings with visual evidence from the intermediate and final simulation states. Again, the machine learning solution represents a minimal fraction of the cost for realizing the numerical approach on grids with larger cell widths. This time, however, it is more difficult for the proposed system to recover the accuracy lost to under-resolution. For example, if the simulation duration increases to $t^{end} = 2$, the hybrid strategy degenerates to being only slightly better than its numerical baseline (see table 4). This vortex test thus reveals the need for improving the training protocol, especially to encompass more patterns from under-resolved regions.

6.3. Stefan problem

Now, we assess the performance of our hybrid algorithm when solving the phase transition of a single-component liquid melt to a solid structure. Here, we consider a diffusion-dominated crystallization process that we can model as

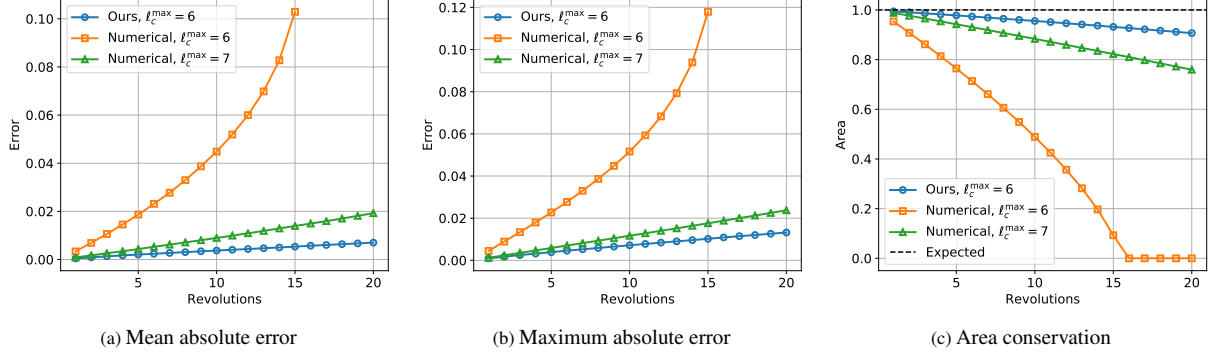


Figure 9: Stress test for the rotation experiment using the ordinary semi-Lagrangian scheme and our hybrid advection system for a mesh size $h_c = 2^{-6}$. For comparison, we also include results for the numerical approach with $h_c = 2^{-7}$. Left and center plots show the ℓ^1 and ℓ^∞ error norms. The plot to the right describes the evolution of the (normalized) area, taking as a reference 7.068583×10^{-2} . (Color online.)

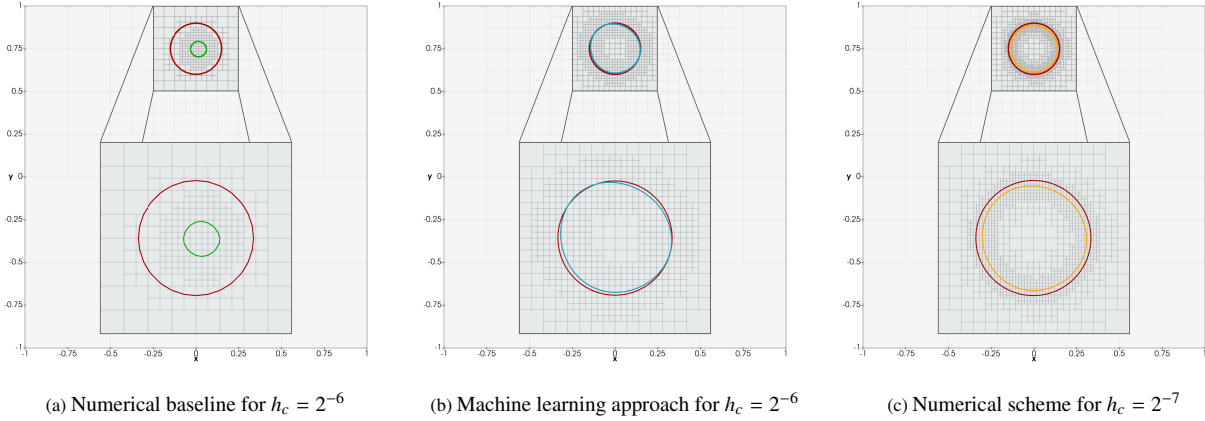


Figure 10: Rotation problem zero level sets at the end of the fifteenth revolution (i.e., $t^{end} = 30\pi\sqrt{2}$). Left and center panels show the numerical baseline in green and the machine-learning-corrected solution in blue for a mesh size $h_c = 2^{-6}$. For comparison, we include the numerical result for a grid with twice the resolution (i.e., $h_c = 2^{-7}$) in the right panel in orange. The analytical disk appears in red for all cases. (Color online.)

a Stefan problem. To state this FBP, suppose we split the computational domain Ω into two subdomains, Ω_s and Ω_l , separated by a solidification front, Γ . The Stefan problem describes the evolution of the scalar temperature field T , decomposed into T_s for the solid phase Ω_s and T_l for the liquid phase Ω_l , as⁹

$$\begin{cases} \frac{\partial T_l}{\partial t} = D_l \Delta T_l, & \text{in } \Omega_l, \\ \frac{\partial T_s}{\partial t} = D_s \Delta T_s, & \text{in } \Omega_s. \end{cases} \quad (21)$$

Generally, the diffusion constants D_l and D_s can be discontinuous across Γ . Moreover, the temperature on the solid-liquid interface satisfies the Gibbs–Thomson boundary condition [91, 92]

$$T_s = T_l = T_\Gamma = -\epsilon_c \kappa - \epsilon_v (\mathbf{u}_{sp} \cdot \mathbf{n}). \quad (22)$$

In this expression, \mathbf{n} is the outward unit vector normal to the solidification front, \mathbf{u}_{sp} denotes the interface velocity, κ is the local curvature at the interface, and ϵ_c and ϵ_v are the surface tension and molecular kinematics supercooling coefficients. As for the normal velocity component, we can compute it in terms of the jump in the heat flux at Γ with

$$\mathbf{u}_{sp} \cdot \mathbf{n} = -[\nabla_{\mathbf{n}} T] = -(D_l \nabla_{\mathbf{n}} T_l - D_s \nabla_{\mathbf{n}} T_s), \quad (23)$$

⁹The subscripts s and l indicate the solid and liquid phases.

Method	ℓ_c^{\max}	MAE	ℓ^∞ error	Disk area	Area loss (%)	Time (sec.)
Ours	6	9.369×10^{-4}	3.751×10^{-3}	7.054×10^{-2}	0.20	0.656
Numerical	6	1.329×10^{-3}	5.686×10^{-3}	6.986×10^{-2}	1.17	0.602
	7	3.367×10^{-4}	2.361×10^{-3}	7.034×10^{-2}	0.49	2.369
	8	9.882×10^{-5}	9.487×10^{-4}	7.059×10^{-2}	0.14	9.715

Table 3: Vortex deformation accuracy and performance assessment. Reported errors include measurements taken at grid points for which $|\phi_{vtx}(\mathbf{x})| \leq \sqrt{2}h_c$ at time $t^{end} = 1.25$.

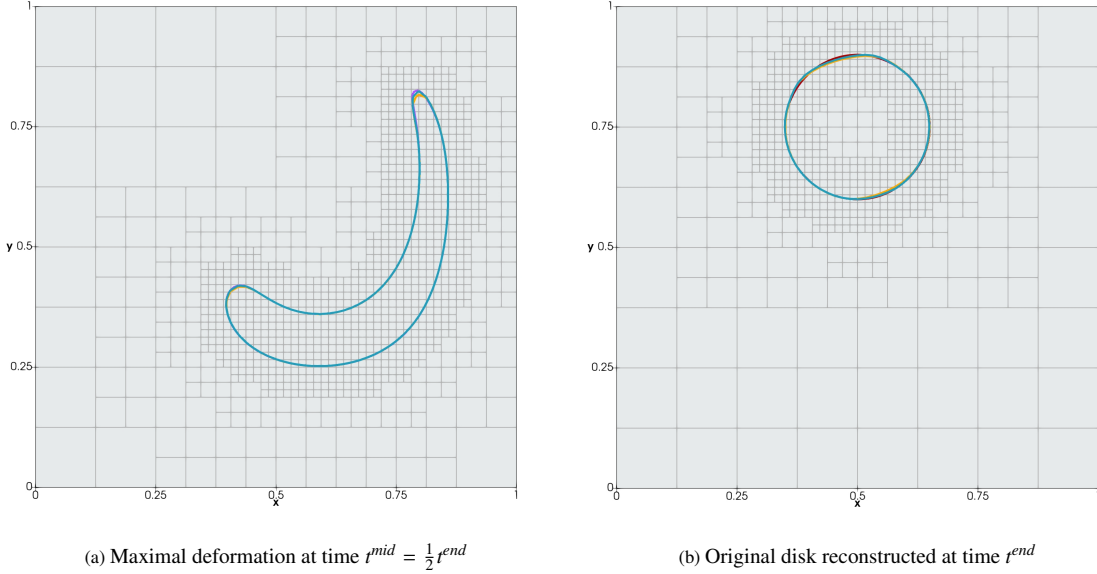


Figure 11: Zero level sets for the vortex experiment at the intermediate and final simulation times. The numerical baseline appears in orange for $\ell_c^{\max} = 6$ and purple for $\ell_c^{\max} = 7$. We show the machine-learning-corrected trajectory in blue for $\ell_c^{\max} = 6$. For comparison, the analytical contour is only visible in the right panel in red. (Color online.)

where $\nabla_{\mathbf{n}}T$ is the directional derivative $\mathbf{n} \cdot \nabla T$. For the practical implementation of the Stefan problem in the parallel level-set framework, we refer the reader to Algorithm 5 in [57]. The latter extends the adaptive-Cartesian-grid-based Algorithm 2 in [55]. In addition, we have assumed $D_s = D_l = 1$ and used PETSc’s BiCGStab KSPSo1ve function [80] to solve the system emerging from eq. (21).

6.3.1. Frank-sphere

First, we evaluate our system’s response to the Frank-sphere problem [93], which has a known analytical solution. In this two-dimensional FBP, a region described by a disk with $T_s = 0$ grows into a supercooled liquid phase. As time progresses, the radius expands according to $R(t) = s_0 \sqrt{t}$, where s_0 is the base parameter. Likewise, we define the temperature field by

$$T(r, t) = T(s) = \begin{cases} 0 & \text{if } s \leq s_0 \\ T_\infty \left(1 - \frac{F(s)}{F(s_0)}\right) & \text{if } s > s_0 \end{cases}, \quad (24)$$

where r is the distance to the disk’s center, $s = r / \sqrt{t}$, and $F(s) = E_1(s^2/4)$. Further, $E_1(z) = \int_z^\infty \frac{e^{-t}}{t} dt$ is the exponential integral, and $F(s)$ is the heat equation’s similarity solution. Also, T_∞ denotes the temperature infinitely far away from Γ . To determine T_∞ , the jump condition in eq. (23) combines with the relation

$$\mathbf{u}_{sp} \cdot \mathbf{n} = \frac{dR}{dt} = \frac{s_0}{2\sqrt{t}} \quad (25)$$

at the freezing front so that

Method	MAE	ℓ^∞ error	Disk area	Area loss (%)
Ours	3.232×10^{-3}	1.164×10^{-2}	7.082×10^{-2}	-0.20
Numerical	4.185×10^{-3}	1.439×10^{-2}	7.021×10^{-2}	0.68

Table 4: Degeneracy in the vortex deformation experiment. Reported errors include measurements taken at grid points for which $|\phi_{vtx}(\mathbf{x})| \leq \sqrt{2}h_c$ at time $t^{end} = 2$ for a mesh size $h_c = 2^{-6}$.

Method	ℓ_c^{\max}	MAE	ℓ^∞ error	Temperature error	Disk area	Area loss (%)	Time (sec.)
Ours	6	5.853×10^{-4}	1.762×10^{-3}	4.225×10^{-4}	6.876×10^{-1}	-0.05	4.342
Numerical	6	8.112×10^{-4}	3.625×10^{-3}	6.982×10^{-4}	6.892×10^{-1}	-0.29	3.497
	7	9.253×10^{-3}	5.614×10^{-2}	9.137×10^{-3}	6.846×10^{-1}	0.38	9.253
	8	5.039×10^{-2}	1.511×10^{-1}	3.405×10^{-2}	6.879×10^{-1}	-0.10	92.190

Table 5: Frank-sphere accuracy and performance statistics. Reported errors include measurements taken at grid points for which $|\phi_{vtx}(\mathbf{x})| \leq \sqrt{2}h_c$ at time $t^{end} = 0.875$.

$$T_\infty = \frac{s_0 F(s_0)}{2F'(s_0)}. \quad (26)$$

In this experiment, $\phi_{fs}(\mathbf{x})$ is our initial level-set function embedded in $\Omega \equiv [-1, +1]^2$ with a circular interface centered at a random location inside $[-h_c/2, +h_c/2]^2$. If we define $s_0 = 0.5$ and $t^0 = 0.25$, we get $T_\infty = -0.15015425523242384$, and the freezing front radius starts at 0.25. With these parameters, we ensure $\max \|\mathbf{u}_{sp}(\mathbf{x})\| \leq 1$ for all $\mathbf{x} \in \Omega$ upon quadratic extension from Γ . In addition, we enforce the time step restriction $\Delta t = h_c$ and the Dirichlet boundary condition $T_\Gamma = 0$.

Table 5 summarizes the interface-location and temperature error statistics for Frank-sphere simulations running until $t^{end} = 0.875$. As before, table 5 also shows the area loss and the running wall time. For comparison, we have included semi-Lagrangian scheme results at resolutions varying from $\ell_c^{\max} = 6$ to $\ell_c^{\max} = 8$. Because of the inherent instability in the Frank-sphere problem, the free boundary grows dendritic structures as the mesh size decreases. However, for $h_c = 2^{-6}$, our strategy agrees with the baseline trajectory while exhibiting better area conservation and temperature accuracy. Figure 12 confirms these observations by contrasting the zero-isocontours computed with the numerical solver and the hybrid system depicted in fig. 3. This test certifies our approach’s feasibility for building solutions for FBPs where the velocity field is not necessarily divergence-free.

6.3.2. Unstable solidification

Last, we evaluate our approach’s response to curvature-driven, anisotropic crystallization. To this end, we place a solid seed into a supercooled liquid and solve eq. (21) with a nonzero Gibbs–Thomson condition (i.e., $T_\Gamma \neq 0$). Here, we consider the domain $\Omega \equiv [-1, +1]^2$ with a temperature field initialized uniformly as $T_l = -0.08$ for the liquid phase and $T_s = 0$ for the seed. The nucleus has a characteristic three-fold freezing front given by the polar rose equation

$$r(\theta) = a \cos(p\theta) + b, \quad (27)$$

where $a = 0.02$, $b = 0.09$, $p = 3$, and $\theta \in [0, 2\pi)$. Furthermore, we have applied the condition in eq. (22) using

$$\epsilon_c = 2 \times 10^{-4} \left[1 + 0.6 \cos \left(4 \left(\theta_n + \frac{\pi}{3} \right) \right) \right] \quad \text{and} \quad \epsilon_v = 0, \quad (28)$$

where θ_n is the interface’s normal vector angle with respect to the horizontal. Also, we have imposed adiabatic boundary conditions for the four sides of Ω . With this configuration, we have carried out the unstable solidification simulation from $t^0 = 0$ to $t^{end} = 3$.

Figures 13 and 14 compare the numerical and machine-learning-corrected growth histories and final zero level sets for the mesh sizes $h_c = 2^{-6}$ and $h_c = 2^{-7}$. Note that in this case, we have used an adaptive time step,

$$\Delta t = h_c \min \left(1, \frac{1}{\max \|\mathbf{u}_{sp}\|} \right), \quad (29)$$

which always leads to an $\mathcal{F}_{6,8}(\cdot)$ -compatible $\Delta t = h_c$ for $\ell_c^{\max} = 6$ but not for $\ell_c^{\max} = 7$. Qualitatively, the results in figs. 13 and 14 show that our hybrid solver converges to the baseline solutions at both levels of refinement. These

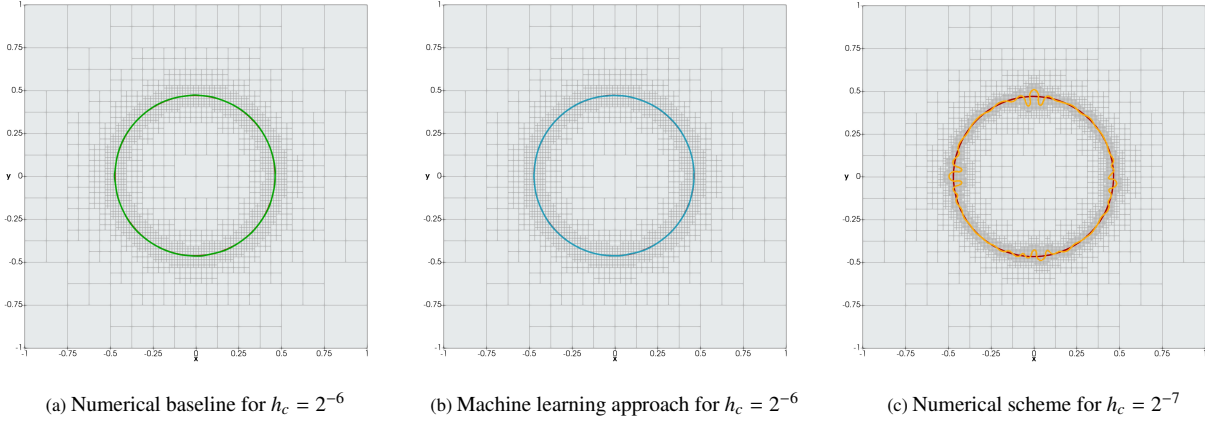


Figure 12: Frank-sphere zero level sets at time $t^{end} = 0.875$. Left and center panels show the numerical baseline in green and the machine-learning-corrected solution in blue for a discretization with $\ell_c^{max} = 6$. For comparison, we include the numerical result for a grid with twice the resolution in the right panel in orange. In all cases, the analytical disk appears in red. (Color online.)

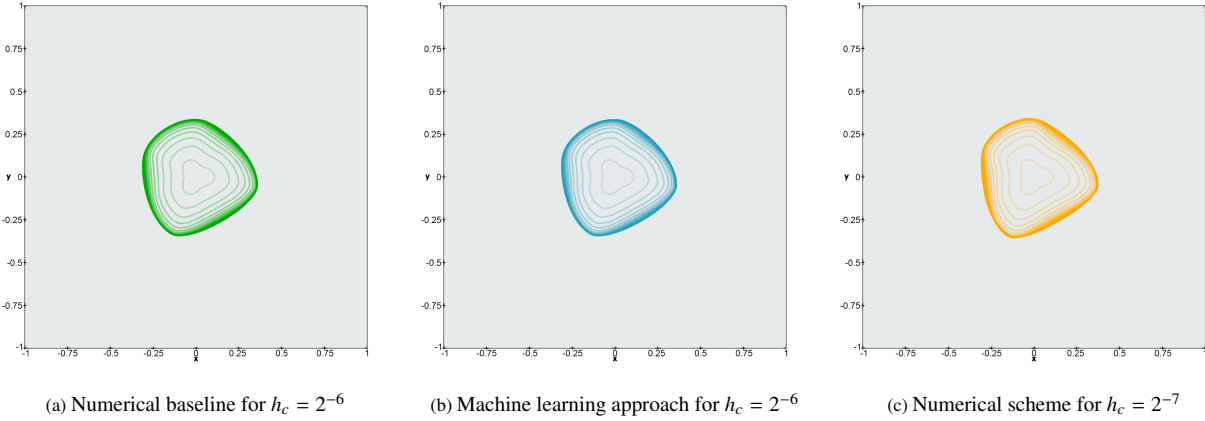


Figure 13: Unstable-solidification zero-level-set growth histories with sixteen steps from $t^0 = 0$ to $t^{end} = 3$ for $\ell_c^{max} = 6, 7$. The numerical trajectories appear in green and orange on the left and right panels. We show our hybrid approach solution in the center chart in blue. (Color online.)

plots thus suggest that our hybrid strategy yields trajectories that agree with the numerical patterns obtained with $\ell_c^{max} = 6$ and $\ell_c^{max} = 7$ for curvature-driven simulations. But, to understand better the machine learning effects on crystallization, further research is necessary to relax the velocity maximum-unit-norm restriction. Possible paths to address this problem involve increasing the variety of speed patterns in \mathcal{D} or introducing velocity embeddings or encoding.

7. Conclusions

We have introduced a hybrid machine learning strategy to improve the accuracy of semi-Lagrangian schemes for relatively coarse adaptive Cartesian grids. Our approach comprises a multilayer perceptron, $\mathcal{F}_{c,f}(\cdot)$, that processes velocity, level-set, and positional information to quantify the error in the interface trajectory. To develop this causal model, we have postulated the problem in terms of the image super-resolution construct [7]. The latter requires employing a high-resolution mesh to supply reference, target level-set values for neural optimization. Once trained, $\mathcal{F}_{c,f}(\cdot)$ operates alongside selective reinitialization and alternates with standard advection to reduce numerical diffusion. Unlike other machine learning solutions for passive scalar transport (e.g., [13, 64–66, 94]), our approach is localized in time and space. In particular, we have avoided complex architectures and evaluations by concentrating our effort only on vertices next to the interface. Also, our error-correcting neural network consumes data just from the current time

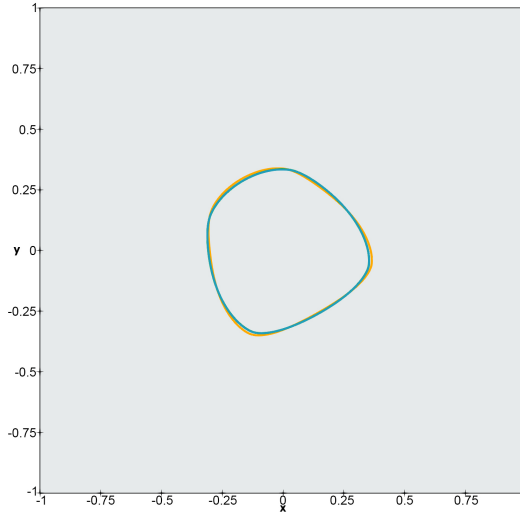


Figure 14: Comparison of the unstable-solidification zero level sets at time $t^{end} = 3$. The numerical interfaces appear in green ($l_c^{\max} = 6$) and orange ($l_c^{\max} = 7$) while our hybrid approach solution is shown in blue for $h_c = 2^{-6}$. Both the machine-learning-corrected and the standard zero-isocontours practically overlap. (Color online.)

frame, thus relieving the system from buffering past states. When taken together, these features make our strategy attractive to modern, parallel level-set frameworks (e.g., [57]), where communication among computing nodes can be expensive.

We have also elaborated on the methodologies to assemble the learning data set and train the error-correcting neural network. Our main contribution is a novel machine-learning-augmented semi-Lagrangian algorithm that blends neural inference with numerically advected level-set values in an alternating fashion. And, to validate its correctness, we have examined the entire strategy with a few representative test cases. These assessments included rotating and warping a disk driven by divergence-free velocity fields and a couple of instances of the Stefan problem. Our test results have confirmed that $\mathcal{F}_{c,f}(\cdot)$ helps to dampen numerical diffusion and improve mass loss in simple advection problems. More precisely, our strategy’s accuracy is often as good as or better than the numerical scheme at twice the resolution while requiring only a fraction of the cost. In the same way, we have shown that our framework produces feasible solidification fronts for crystallization processes. However, bias artifacts and significant deterioration have occurred in lengthy or particularly deforming simulations. In addition, the stringent velocity maximum-unit-norm condition imposes severe limitations, especially for FBPs involving rapid interface changes.

Unwelcome artifacts, unexpected results, and limitations in our case studies reveal several opportunities for future investigation. For example, we could enrich the learning data set by incorporating more than a single interface type (e.g., sine waves, as in [45]) and more velocity patterns while emphasizing under-resolved sampling. Other promising avenues for enhancing robustness involve binding physical constraints to $\mathcal{F}_{c,f}(\cdot)$ [24–26, 95], integrating velocity embeddings, adversarial training [8, 13, 94], and even replacing the semi-Lagrangian formulation for another more accurate method. Similarly, we could consider temporal data only if it does not set back `MLSemLagrangian()`’s performance. Finally, migrating our strategy to higher resolutions and three-dimensional domains is a challenging problem on its own, too. Echoing the arguments and motivation in [66], we thus hope our contributions here open up further interdisciplinary research between machine learning and scientific computing.

Acknowledgements

Use was made of computational facilities purchased with funds from the National Science Foundation (CNS-1725797) and administered by the Center for Scientific Computing (CSC). The CSC is supported by the California NanoSystems Institute and the Materials Research Science and Engineering Center (MRSEC; NSF DMR 1720256) at UC Santa Barbara.

References

- [1] C. C. Aggarwal. *Neural Networks and Deep Learning – A Textbook*. Springer, Cham, 2018.
- [2] P. Mehta, M. Bukov, C. Wang, A. G. R. Day, C. Richardson, C. K. Fisher, and D. J. Schwab. A high-bias, low-variance introduction to machine learning for physicists. *Phys. Rep.*, 810:1–124, May 2019.
- [3] A. Gerón. *Hands-on Machine Learning with Scikit-Learn, Keras & TensorFlow: Concepts, Tools, and Techniques to Build Intelligent Systems*. O’Reilly, 2nd edition, November 2019.
- [4] M. Turk and A. Pentland. Eigenfaces for recognition. *J. Cogn. Neurosci.*, 3(1):71–86, 1991.
- [5] P. Vincent, H. Larochelle, I. Lajoie, Y. Bengio, and P.-A. Manzagol. Stacked denoising autoencoders: Learning useful representations in a deep network with a local denoising criterion. *J. Mach. Learn. Res.*, 11:3371–3408, December 2010.
- [6] A. Krizhevsky, I. Sutskever, and G. Hinton. Imagenet classification with deep convolutional neural networks. In *NIPS Conference*, pages 1097–1105, 2012.
- [7] C. Dong, C. C. Loy, K. He, and X. Tang. Learning a deep convolutional network for image super-resolution. In D. Fleet, T. Pajdla, B. Schiele, and T. Tuytelaars, editors, *Computer Vision – ECCV 2014*, pages 184–199, Cham, 2014. Springer International Publishing.
- [8] I. Goodfellow, J. Pouget-Abadie, M. Mirza, B. Xu, D. Warde-Farley, S. Ozair, A. Courville, and Y. Bengio. Generative adversarial nets. In Z. Ghahramani, M. Welling, C. Cortes, N. D. Lawrence, and K. Q. Weinberger, editors, *Proc. NeurIPS 27*, pages 2672–2680. Curran Associates, Inc., 2014.
- [9] O. Ronneberger, P. Fischer, and T. Brox. U-Net: Convolutional networks for biomedical image segmentation. In N. Navab, J. Hornegger, W. M. Wells, and A. F. Frangi, editors, *Medical Image Computing and Computer-Assisted Intervention – MICCAI 2015*, pages 234–241, Cham, 2015. Springer International Publishing.
- [10] K. He, X. Zhang, S. Ren, and J. Sun. Deep residual learning for image recognition. In *CVPR*, pages 770–778, 2016.
- [11] T. A. Ngo, Z. Lu, and G. Carneiro. Combining deep learning and level set for the automated segmentation of the left ventricle of the heart from cardiac cine magnetic resonance. *Medical Image Analysis*, 35:159–171, January 2017.
- [12] T. H. N. Le, K. G. Quach, K. Luu, C. N. Duong, and M. Savvides. Reformulating level sets as deep recurrent neural network approach to semantic segmentation. *IEEE Trans. on Image Process.*, 27(5):2393–2407, May 2018.
- [13] Y. Xie, E. Franz, M. Chu, and N. Thuerey. tempoGAN: A temporally coherent, volumetric GAN for super-resolution fluid flow. *ACM Trans. Graph.*, 37(4):1–15, July 2018.
- [14] T. Mikolov, I. Sutskever, K. Chen, G. S. Corrado, and J. Dean. Distributed representations of words and phrases and their compositionality. In C. J. C. Burges, L. Bottou, M. Welling, Z. Ghahramani, and K. Q. Weinberger, editors, *NeurIPS 26*, pages 3111–3119. Curran Associates, Inc., 2013.
- [15] P. Bojanowski, E. Grave, A. Joulin, and T. Mikolov. Enriching word vectors with subword information. In *Trans. Assoc. Comput. Linguist.*, volume 5, pages 135–146, 2017.
- [16] M. E. Peters, M. Neumann, M. Iyyer, M. Gardner, C. Clark, K. Lee, and L. Zettlemoyer. Deep contextualized word representations. In *Proc. of NAACL*, 2018.
- [17] S. Arora, Y. Liang, and T. Ma. A simple but tough-to-beat baseline for sentence embeddings. In *Proc. ICLR*, April 2017.
- [18] S. Hochreiter and J. Schmidhuber. Long short-term memory. *Neural Comput.*, 9(8):1735–1780, November 1997.

- [19] K. Cho, B. V. Merriënboer, Ç. Gülçehre, D. Bahdanau, F. Bougares, H. Schwenk, and Y. Bengio. Learning phrase representations using RNN encoder-decoder for statistical machine translation. In *Proc. EMNLP*, 2014.
- [20] A. Vaswani, N. Shazeer, N. Parmar, J. Uszkoreit, L. Jones, A. N. Gomez, Ł. Kaiser, and I. Polosukhin. Attention is all you need. In I. Guyon, U. V. Luxburg, S. Bengio, H. Wallach, R. Fergus, S. Vishwanathan, and R. Garnett, editors, *NeurIPS 30*, pages 5998–6008. Curran Associates, Inc., 2017.
- [21] N. Yadav, A. Yadav, and M. Kumar. *An Introduction to Neural Network Methods for Differential Equations*. SpringerBriefs in Computational Intelligence. Springer Netherlands, 2015.
- [22] I. E. Lagaris, A. Likas, and D. I. Fotiadis. Artificial neural networks for solving ordinary and partial differential equations. *IEEE Trans. Neural Netw.*, 9(5):987–1000, 1998.
- [23] I. E. Lagaris, A. C. Likas, and D. G. Papageorgiou. Neural-network methods for boundary value problems with irregular boundaries. *IEEE Trans. Neural Netw.*, 11(5):1041–1049, September 2000.
- [24] M. Raissi, P. Perdikaris, and G. E. Karniadakis. Physics informed deep learning (part I): Data-driven solution of nonlinear partial differential equations. <https://arxiv.org/abs/1711.10561>, November 2017.
- [25] M. Raissi. Deep hidden physics models: Deep learning of nonlinear partial differential equations. *J. Mach. Learn. Res.*, 19(25):1–24, 2018.
- [26] M. Raissi, P. Perdikaris, and G. E. Karniadakis. Physics-informed neural networks: A deep learning framework for solving forward and inverse problems involving nonlinear partial differential equations. *J. Comp. Phys.*, 378:686–707, February 2019.
- [27] W.-F. Hu, T.-S. Lin, and M.-C. Lai. A discontinuity capturing shallow neural network for elliptic interface problems. <https://arxiv.org/abs/2106.05587>, June 2021.
- [28] S. Pakravan, P. Mistani, M. A. Aragon-Calvo, and F. Gibou. Solving inverse-PDE problems with physics-aware neural networks. *J. Comput. Phys.*, 440(4):110414, September 2021.
- [29] D. Ray and J. S. Hesthaven. An artificial neural network as a troubled-cell indicator. *J. Comp. Phys.*, 367:166–191, April 2018.
- [30] N. R. Morgan, S. Tokareva, X. Liu, and A. D. Morgan. A machine learning approach for detecting shocks with high-order hydrodynamic methods. *AIAA SciTech Forum*, January 2020.
- [31] A. B. Buhendwa, D. A. Bezgin, and N. Adams. Consistent and symmetry preserving data-driven interface reconstruction for the level-set method. <https://arxiv.org/abs/2104.11578>, April 2021.
- [32] A. Friedman. *Variational Principles of Free-Boundary Problems*. Dover Publications, 2010.
- [33] C. W. Hirt and B. D. Nichols. Volume of fluid (VOF) method for the dynamics of free boundaries. *J. Comput. Phys.*, 39:201–225, 1981.
- [34] A. Fasano and M. Primicerio, editors. *Free Boundary Problems: Theory and Applications*. Pitman, Boston, 1983.
- [35] J. S. Langer. *Models of Pattern Formation in First-Order Phase Transitions*. Number 165-186. World Scientific, 1986.
- [36] S. Osher and J. A. Sethian. Fronts propagating with curvature-dependent speed: Algorithms based on Hamilton–Jacobi formulations. *J. Comput. Phys.*, 79:12–49, 1988.
- [37] B. Després and H. Jourdain. Machine learning design of volume of fluid schemes for compressible flows. *J. Comput. Phys.*, 408(1):109275, May 2020.
- [38] Y. Qi, J. Lu, R. Scardovelli, S. Zaleski, and G. Tryggvason. Computing curvature for volume of fluid methods using machine learning. *J. Comput. Phys.*, 377:155–161, 2019.
- [39] H. V. Patel, A. Panda, J. A. M. Kuipers, and E. A. J. F. Peters. Computing interface curvature from volume fractions: A machine learning approach. *Comput. & Fluids*, 193:104263, October 2019.

- [40] M. Ataei, M. Bussmann, V. Shaayegan, F. Costa, S. Han, and C. B. Park. NPLIC: A machine learning approach to piecewise linear interface construction. <https://arxiv.org/abs/2007.04244>, January 2021.
- [41] D. Youngs. Time-dependent multi-material flow with large fluid distortion. *Num. Method Fluid Dyn.*, 24:273–285, January 1982.
- [42] S. Popinet. Numerical models of surface tension. *Annu. Rev. Fluid Mech.*, 50(1):49–75, January 2018.
- [43] M. Moog, R. Keck, and A. Zemitis. Some numerical aspects of the level set method. *Math. Model. Anal.*, 3(1):140–151, 1998.
- [44] M. Sussman and E. G. Puckett. A coupled level set and volume-of-fluid method for computing 3D and axisymmetric incompressible two-phase flows. *J. Comput. Phys.*, 162(2):301–337, August 2000.
- [45] L. Á. Larios-Cárdenas and F. Gibou. A deep learning approach for the computation of curvature in the level-set method. *SIAM J. Sci. Comput.*, 43(3):A1754–A1779, January 2021.
- [46] L. Á. Larios-Cárdenas and F. Gibou. A hybrid inference system for improved curvature estimation in the level-set method using machine learning. <https://arxiv.org/abs/2104.02951>, June 2021.
- [47] M. Berger and J. Olinger. Adaptive mesh refinement for hyperbolic partial differential equations. *J. Comput. Phys.*, 53(3):484–512, March 1984.
- [48] J. Strain. Tree methods for moving interfaces. *J. Comput. Phys.*, 151(2):616–648, May 1999.
- [49] C. Min and F. Gibou. A second order accurate projection method for the incompressible Navier–Stokes equations on non-graded adaptive grids. *J. Comput. Phys.*, 219(2):912–929, December 2006.
- [50] C. Min, F. Gibou, and H. Ceniceros. A supra-convergent finite difference scheme for the variable coefficient Poisson equation on non-graded grids. *J. Comput. Phys.*, 218(1):123–140, October 2006.
- [51] C. Min and F. Gibou. A second order accurate level set method on non-graded adaptive Cartesian grids. *J. Comput. Phys.*, 225(1):300–321, July 2007.
- [52] H. Chen, C. Min, and F. Gibou. A supra-convergent finite difference scheme for the Poisson and heat equations on irregular domains and non-graded adaptive Cartesian grids. *J. Sci. Comput.*, 31(1-2):19–60, March 2007.
- [53] C. Min and F. Gibou. Geometric integration over irregular domains with application to level-set methods. *J. Comput. Phys.*, 226(2):1432–1443, October 2007.
- [54] C. Min and F. Gibou. Robust second-order accurate discretizations of the multi-dimensional Heaviside and Dirac delta functions. *J. Comput. Phys.*, 227(22):9686–9695, November 2008.
- [55] H. Chen, C. Min, and F. Gibou. A numerical scheme for the Stefan problem on adaptive Cartesian grids with supralinear convergence rate. *J. Comput. Phys.*, 228(16):5803–5818, September 2009.
- [56] C. Burstedde, L. C. Wilcox, and O. Ghattas. p4est: Scalable algorithms for parallel adaptive mesh refinement on forests of octrees. *SIAM J. Sci. Comput.*, 33(3):1103–1133, May 2011.
- [57] M. Mirzadeh, A. Guittet, C. Burstedde, and F. Gibou. Parallel level-set methods on adaptive tree-based grids. *J. Comput. Phys.*, 322:345–364, 2016.
- [58] D. Enright, R. Fedkiw, J. Ferziger, and I. Mitchell. A hybrid particle level set method for improved interface capturing. *J. Comput. Phys.*, 183(1):83–116, 2002.
- [59] D. L. Sun and W. Q. Tao. A coupled volume-of-fluid and level set (VOSET) method for computing incompressible two-phase flows. *Int. J. Heat Mass Transf.*, 53(4):645–655, January 2010.
- [60] V. Mihalef, D. Metaxas, and M. Sussman. Textured liquids based on the marker level set. *Comput. Graph. Forum*, 26(3):457–466, September 2007.

- [61] A. Salih and S. Ghosh-Moulic. A mass conservation scheme for level set method applied to multiphase incompressible flows. *Int. J. Comput. Meth. Eng. Sci. Mech.*, 14(4):271–289, May 2013.
- [62] H.-Z. Yuan, C. Shu, Y. Wang, and S. Shu. A simple mass-conserved level set method for simulation of multiphase flows. *Phys. Fluids*, 30(4):040908, March 2018.
- [63] Y. Bar-Sinai, S. Hoyer, J. Hickey, and M. P. Brenner. Learning data-driven discretizations for partial differential equations. *PNAS*, 116(31):15344–15349, July 2019.
- [64] J. Zhuang, D. Kochkov, Y. Bar-Sinai, M. P. Brenner, and S. Hoyer. Learned discretizations for passive scalar advection in a two-dimensional turbulent flow. *Phys. Rev. Fluids*, 6(6):064605, June 2021. <https://github.com/google-research/data-driven-advection>.
- [65] B. Liu, J. Tang, H. Huang, and X.-Y. Lu. Deep learning methods for super-resolution reconstruction of turbulent flows. *Phys. Fluids*, 32(2):025105, February 2020.
- [66] J. Pathak, M. Mustafa, K. Kashinath, E. Motheau, T. Kurth, and M. Day. Using machine learning to augment coarse-grid computational fluid dynamics simulations. <https://arxiv.org/abs/2010.00072>, 2020.
- [67] R. Courant, E. Isaacson, and M. Rees. On the solution of nonlinear hyperbolic differential equations by finite differences. *Comm. Pure Appl. Math.*, 5:243–255, 1952.
- [68] A. Wiin-Nielsen. On the application of trajectory methods in numerical forecasting. *Tellus*, 11(2):180–196, 1959.
- [69] S. J. Fletcher. *Semi-Lagrangian Advection Methods and Their Applications in Geoscience*. Elsevier, Amsterdam, Netherlands; Oxford, England; Cambridge, Massachusetts, 2020.
- [70] M. Sussman, P. Smereka, and S. Osher. A level set approach for computing solutions to incompressible two-phase flow. *J. Comput. Phys.*, 114(1):146–159, September 1994.
- [71] C. Min. On reinitializing level set functions. *J. Comp. Phys.*, 229(8):2764–2772, April 2010.
- [72] S. Osher and R. Fedkiw. *Level Set Methods and Dynamic Implicit Surfaces*. Appl. Math. Sci. 153. Springer, Cham, 2002.
- [73] J. A. Sethian. *Level Set Methods and Fast Marching Methods*. Cambridge Monogr. Appl. Comput. Math. Cambridge University Press, Cambridge, UK, 2nd edition, 1999.
- [74] F. Gibou, R. Fedkiw, and S. Osher. A review of level-set methods and some recent applications. *J. Comput. Phys.*, 353:82–109, 2018.
- [75] M. de Berg, M. van Kreveld, M. Overmars, and O. Schwarzkopf. *Computational Geometry - Algorithms and Applications*. Springer, Cham, 2nd edition, 2000.
- [76] C. Min. Local level set method in high dimension and codimension. *J. Comput. Phys.*, 200:368–382, 2004.
- [77] W. Gropp, E. Lusk, and A. Skjellum. *Using MPI: Portable Parallel Programming with the Message-Passing Interface*. MIT Press, Cambridge, MA, 3rd edition, 2014.
- [78] D. Xiu and G. Karniadakis. A semi-Lagrangian high-order method for Navier–Stokes equations. *J. Comput. Phys.*, 172(2):658–684, September 2001.
- [79] D. S. Parker. Exploring the Matrix – Adventures in Modeling with Matlab. UCLA Course Reader Solutions, January 2016.
- [80] S. Balay, S. Abhyankar, M. F. Adams, J. Brown, P. Brune, K. Buschelman, L. Dalcin, A. Dener, V. Eijkhout, W. D. Gropp, D. Karpeyev, D. Kaushik, M. G. Knepley, D. A. May, L. Curfman McInnes, R. Tran Mills, T. Munson, K. Rupp, P. Sanan, B. F. Smith, S. Zampini, H. Zhang, and H. Zhang. PETSc. <https://www.mcs.anl.gov/petsc>, 2019.

- [81] T. Saad and J. C. Sutherland. Comment on “Diffusion by a random velocity field” [Phys. Fluids 13, 22 (1970)]. *Phys. Fluids*, 28(11):119101, December 2016.
- [82] M. Abadi, A. Agarwal, P. Barham, E. Brevdo, Z. Chen, C. Citro, G. S. Corrado, A. Davis, J. Dean, M. Devin, S. Ghemawat, I. Goodfellow, A. Harp, G. Irving, M. Isard, R. Jozefowicz, Y. Jia, L. Kaiser, M. Kudlur, J. Levenberg, D. Mané, M. Schuster, R. Monga, S. Moore, D. Murray, C. Olah, J. Shlens, B. Steiner, I. Sutskever, K. Talwar, P. Tucker, V. Vanhoucke, V. Vasudevan, F. Viégas, O. Vinyals, P. Warden, M. Wattenberg, M. Wicke, Y. Yu, and X. Zheng. TensorFlow: Large-Scale Machine Learning on Heterogeneous Systems. <https://www.tensorflow.org>, 2015.
- [83] F. Chollet et al. Keras. <https://keras.io>, 2015.
- [84] F. Pedregosa, G. Varoquaux, A. Gramfort, V. Michel, B. Thirion, O. Grisel, M. Blondel, P. Prettenhofer, R. Weiss, V. Dubourg, J. Vanderplas, A. Passos, D. Cournapeau, M. Brucher, M. Perrot, and E. Duchesnay. Scikit-learn: Machine learning in Python. *J. Mach. Learn. Res.*, 12:2825–2830, 2011.
- [85] W. McKinney. Data Structures for Statistical Computing in Python. In S. van der Walt and J. Millman, editor, *Proceedings of the 9th Python in Science Conference*, pages 56–61, 2010. <https://pandas.pydata.org>.
- [86] Y. A. LeCun, L. Bottou, G. B. Orr, and K.-R. Müller. *Efficient BackProp*, volume 7700 of *Lecture Notes in Comput. Sci.*, pages 9–48. Springer Berlin Heidelberg, Berlin, Heidelberg, 2012.
- [87] N. Lohmann. JSON for modern C++. <https://github.com/nlohmann/json>, August 2020. v3.9.1.
- [88] T. Hermann. Frugally-deep. <https://github.com/Dobiasd/frugally-deep>, February 2021. v0.15.2.
- [89] Z. Xianyi and M. Kroeker. OpenBLAS: An optimized BLAS library. <https://github.com/xianyi/OpenBLAS>, July 2021. v0.3.17.
- [90] J. B. Bell, P. Colella, and H. M. Glaz. A second order projection method for the incompressible Navier–Stokes equations. *J. Comput. Phys.*, 85(2):257–283, December 1989.
- [91] V. Alexiades, A. D. Solomon, and D. G. Wilson. The formation of a solid nucleus in supercooled liquid, I. *J. Non-Equilib. Thermodyn.*, 13:281–300, 1988.
- [92] V. Alexiades and A. D. Solomon. *Mathematical Modeling of Melting and Freezing Processes*. Hemisphere, Washington, DC, 1st edition, 1993.
- [93] F. C. Frank. Radially symmetric phase growth controlled by diffusion. *Proc. Royal Soc. A*, 201(1067):586–599, May 1950.
- [94] A. B. Farimani, J. Gomes, and V. S. Pande. Deep learning the physics transport phenomena. <https://arxiv.org/abs/1709.02432>, September 2017.
- [95] T. Beucler, M. Pritchard, S. Rasp, J. Ott, P. Baldi, and P. Gentine. Enforcing analytic constraints in neural networks emulating physical systems. *Phys. Rev. Lett.*, 126(9):098302, March 2021.